STATE OF THE CLIMATE IN 2010

J. Blunden, D. S. Arndt, and M. O. Baringer, Eds.

Associate Eds. H. J. Diamond, A. J. Dolman, R. L. Fogt, B. D. Hall, M. Jeffries, J. M. Levy, J. Richter-Menge, J. M. Renwick, P. W. Thorne, L. A. Vincent, and K. M. Willett,

Special Supplement to the
Bulletin of the American Meteorological Society
Vol. 92, No. 6, June 2011

3. GLOBAL OCEANS—J. M. Levy, Ed.

a. Overview—E. J. Kearns and J. M. Levy

Calendar year 2010 exhibited anomalies in ocean temperature, salinity, sea level, heat content, currents, carbon, and phytoplankton that were highly influenced by the transition from El Niño to La Niña conditions in the Pacific Ocean, maintenance of a negative phase of the North Atlantic Oscillation, and transition to a negative phase of the Pacific Decadal Oscillation. Consequentially, the state of the ocean climate in 2010 was characterized by relatively anomalous patterns compared with climatologies and with the previous calendar year. The following highlights are fully described in the chapter that follows:

- The global sea surface temperature variations observed in 2010 were characterized by the transition from El Niño to La Niña during the summer 2010, the development of a negative Pacific Decadal Oscillation pattern in the North Pacific during the fall/winter of 2010, and the development of a tripole sea surface temperature (SST) anomaly pattern in the North Atlantic.
- Global integrals of upper ocean heat content for the past several years have reached values consistently higher than for all prior times in the historical record, consistent with the dominant role of the ocean in the Earth's net energy uptake. Deep and abyssal waters of Antarctic origin have also trended warmer on average since the early 1990s.
- The global ocean latent and sensible heat fluxes in 2010 reflected a primary role of near-surface wind anomalies in causing heat flux anomalies; the latter, in turn, served as a forcing mechanism for many of the SST anomalies in the North Atlantic and the tropical Indian and western Pacific Oceans. The globally-averaged heat flux from the ocean was close to that in 2009, remaining below the peak value seen about a decade ago.
- The sea surface became saltier in 2010 relative to 2009 in the western equatorial Pacific, and fresher in the central equatorial Pacific, mostly owing to an eastward shift in convection and precipitation associated with El Niño. Overall, saltier (higher evaporation) regions of the ocean surface continue to be anomalously salty, and fresher (higher precipitation) regions anomalously fresh in 2010. This pattern, which has held over the last several decades, suggests an increase in the hydrological cycle, consistent with climate model predictions for a warming atmosphere. Changes between 2009 and 2010 in subsurface salinity of 0.02–0.04 (Practical Salinity Scale) have occurred in the upper 1000 m of all three major ocean basins.
- Westward La Niña-associated surface current anomalies in the equatorial Pacific were the strongest seen in the last decade. The Kuroshio shifted northward compared with the previous four years, and an anomalously high North Brazil Current shed rings into the Northern Hemisphere.
- The meridional overturning circulation shows no statistically significant trend between April 2004 and April 2009, and there are no unusual anomalous features of note. A significant surface component of this circulation, the Florida Current, has continued the slight decrease observed over the past four years, and now falls within its lowest 25% of all annual mean values from the 29-year record.
- The effects of negative Pacific Decadal Oscillation and North Atlantic Oscillation states are evident in regional sea level changes in the North Pacific and North Atlantic during 2010, as well as in extreme coastal sea level amplitudes with above-normal levels off the west coast of North America and below-normal levels in Northern Europe.
- The global net carbon uptake flux for the 2009 transition period from La Niña to El Niño conditions is estimated to be 1.40 Pg C yr^{-1}, very similar to the 27-year mean. A recent synthesis suggests that, between 1800 and 2008, up to 8.2 Pg C accumulated in the marginal seas, i.e., approximately 6% of the global ocean storage of 148 Pg C.
- Estimates of chlorophyll trends were derived from the SeaWiFS sensor, whose 13-year mission ended in December 2010. A statistically-significant, decadal decrease in chlorophyll concentration at midlatitudes reflects the trend in positive SST anomalies. The cool Southern Ocean shows an increase in concentrations that may be tied to a decrease in mean SST in that region. Historical in situ studies confirm the signs of the trends but suggest a larger rate of change than that derived from SeaWiFS.

b. Sea surface temperatures—Y. Xue, R. W. Reynolds, V. Banzon, T. M. Smith, and N. A. Rayner

The global sea surface temperature (SST) variations in 2010 were characterized by: (1) the transition from El Niño to La Niña during the boreal summer 2010; (2) the development of a negative Pacific Decadal Oscillation (PDO) pattern (Mantua et al. 1997) in the North Pacific during the fall and winter 2010; and (3) the development of a tripole SST anomaly (SSTA) pattern in the North Atlantic. To quantify uncertainties in SSTA, three SST products were used: (1) the Optimal Interpolation SST version 2 (OISST; Reynolds et al. 2002); (2) the Extended Reconstructed SST version 3b (ERSST; Smith et al. 2008); and (3) the UK Met Office Hadley Centre sea ice and SST dataset (HadISST1; Rayner et al. 2003). The OISST is a satellite-based analysis that uses in situ data for bias adjustments of the satellite data for the period since November 1981, when satellite AVHRR became available. The ERSST and HadISST1 analyses are historical analyses beginning in the 19th century, and both analyses use statistics from the more recent period that includes satellite data. The ERSST includes in situ data only, while the HadISST1 includes both in situ measurements and AVHRR retrievals from 1982 onwards.

In this section, SSTA is defined as departure from the 1981–2010 climatology, which was recently constructed to meet the World Meteorological Organization's standard for climatology to reflect the most recent 30-year period (http://www.wmo.int/pages/prog/wcp/wcdmp/documents/WCDMPNo61.pdf). The 1981–2000 climatology, which was utilized in past *State of the Climate* reports, is about 0.2°C higher than the 1971–2000 climatology (Xue et al. 2003) over much of the tropical oceans and North Atlantic (see details in http://www.cpc.ncep.noaa.gov/products/people/yxue/sstclim/Note_SST_Climatology_1981-2010.doc).

The yearly mean SSTA in 2010 was characterized by negative SSTA in the tropical central and tropical eastern Pacific (Fig. 3.1a), reflecting the dominant influence of La Niña (see section 4b). Outside of the tropical Pacific, the 2010 SSTA was characterized by a negative PDO pattern in the North Pacific, a tripole pattern in the North Atlantic, and general warmth in the Indian Ocean, the central-west South Pacific, and the South Atlantic (Fig. 3.1a). The 2010 minus 2009 SST differences show a cooling of about 1°C in the central and eastern tropical Pacific related to the transition from El Niño to La Niña, a moderate cooling in the midlatitude eastern North Pacific, a strengthening of the tripole SSTA in the North Atlantic and a moderate warming near the Maritime Continents, in the midlatitude southern Indian Ocean and central-west South Pacific (Fig. 3.1b).

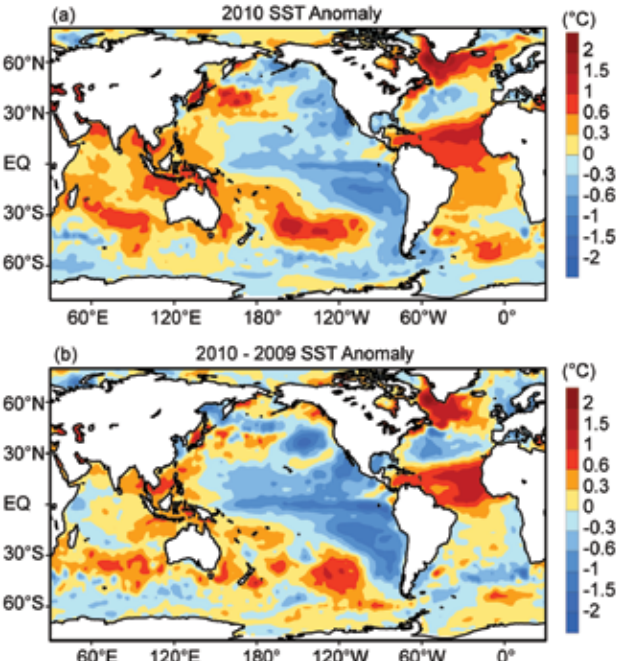

Fig. 3.1. (a) Yearly mean OISST anomaly in 2010, (b) 2010 minus 2009 OISST anomaly.

The evolution of seasonal mean SSTA in 2010 is shown in Fig. 3.2. Positive SSTA dominated in the central tropical Pacific during the winter 2009/10 (December–February) with an amplitude of more than +1.5°C (Fig. 3.2a). By the spring (March–May) 2010, SST had returned to near-normal conditions in the eastern tropical Pacific while SST remained weakly above normal west of 150°W (Fig. 3.2b). Negative SSTA developed and covered the equatorial Pacific east of 170°E during the summer (June–August), indicative of development of La Niña conditions (Fig. 3.2c). At the same time, a negative PDO pattern developed, characterized by positive SSTA (more than +1.0°C) in the midlatitude western and central North Pacific and negative SSTA (less than -1.0°C) extending from the central tropical Pacific to the west coast of North America and Gulf of Alaska (Fig. 3.2c). The negative SSTA near the Gulf of Alaska and along the North America west coast were associated with enhanced upwelling and anomalous anticyclonic winds in the northeast Pacific. During the fall (September–November), negative SSTA strengthened in the central and eastern tropical Pacific, while negative SSTA near the Gulf of Alaska weakened associated with suppressed upwelling.

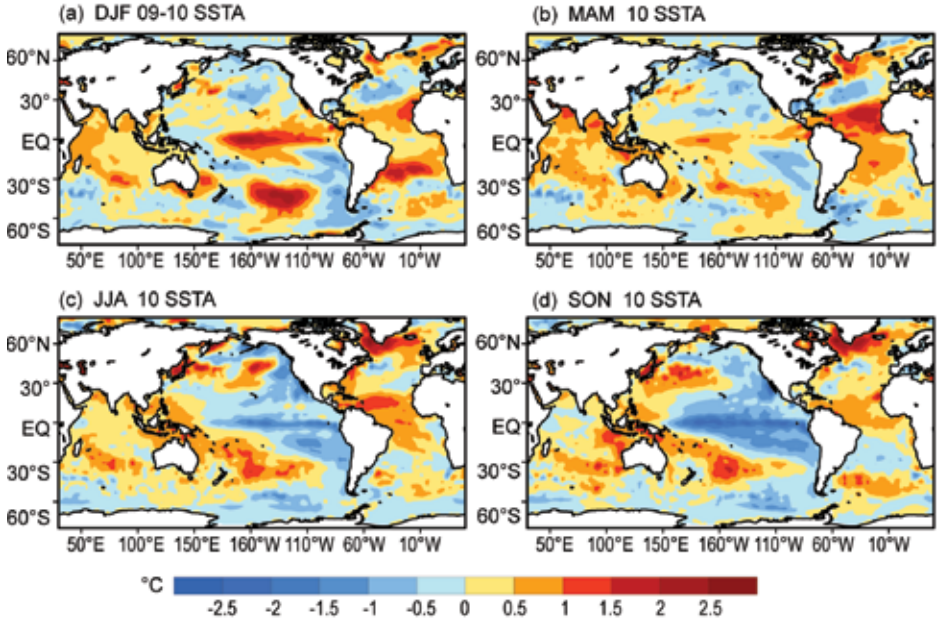

Fig. 3.2. Seasonal mean SSTAs (°C) for (a) December 2009–February 2010, (b) March–May 2010, (c) June–August 2010 and (d) September–November 2010. SSTs are the monthly fields temporally averaged from the weekly 1° OISST.

Positive (negative) SSTA usually appear in ocean basins away from the Pacific approximately three to six months after El Niño (La Niña) peaks in the tropical Pacific (Klein et al. 1999; Enfield and Mayer 1997); due to the remote impacts of the El Niño, positive SSTA strengthened in the tropical Indian Ocean and tropical North Atlantic during the spring 2010 (Fig. 3.2b). In fact, the SST in the tropical North Atlantic reached a historical high during the spring and summer 2010 that has been attributed to combined forcing from the El Niño, the persistent negative phase of the North Atlantic Oscillation (NAO; Fig. 3.3a) and the long-term trend (Hu et al. 2011). Positive SSTA in the tropical Indian Ocean weakened gradually from values higher than +0.5°C during the spring to less than 0°C during the fall 2010 in the western and central tropical Indian Ocean (Figs. 3.2b–d). The cooling is probably associated with the remote impacts of La Niña.

The tripole SSTA in the North Atlantic, characterized by positive (negative) SSTA in the subtropics and high latitudes (midlatitudes), developed during the winter of 2009/10 and spring 2010 (Figs. 3.2a,b), and strengthened during the summer and fall, due to substantial warming in the subpolar region (Figs. 3.2c,d). Figure 3.3 shows the evolution of the zonal average SSTA in the North Atlantic along with the NOAA Climate Prediction Center's NAO index from January 2009 to December 2010. There is a southward propagation of negative (positive) SSTA from high latitudes to midlatitudes (midlatitudes to subtropics) during the latter half of 2009. Those anomalies evolved into a tripole SSTA in which positive (negative) SSTA in the subtropics (midlatitudes) strengthened, and positive SSTA developed in high latitudes (Fig. 3.3b). The warming of the subtropical North Atlantic SST in the early spring can be attributed to the combined forcings from the El Niño and a persistent negative NAO that often warms the

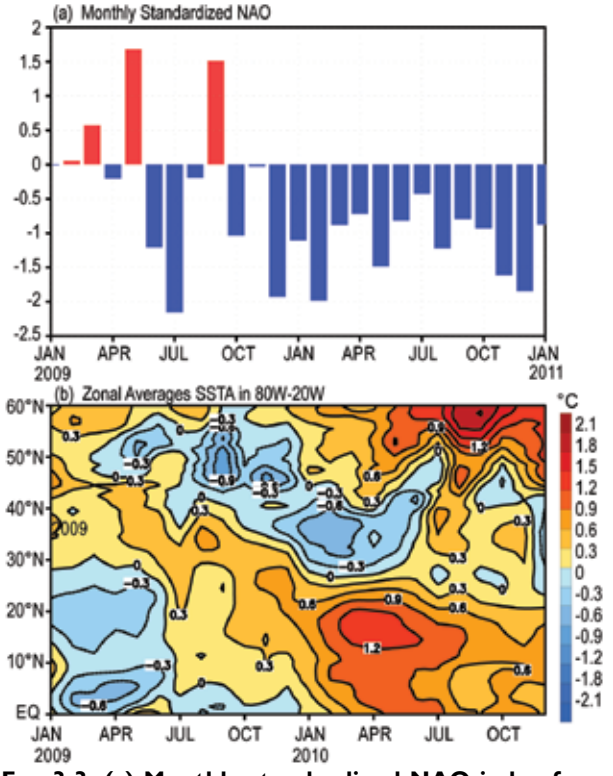

Fig. 3.3. (a) Monthly standardized NAO index from http://www.cpc.ncep.noaa.gov. (b) Time-Latitude section of SST anomalies averaged between 80°W and 20°W. SSTs are the monthly fields temporally averaged from the weekly 1° OISST.

SST in the subtropics and high latitudes, and cools the SST in midlatitudes by modifying evaporative heat loss from the ocean (Deser and Blackmon 1993). Positive SSTA in the subtropics decayed rapidly from +1.2°C in April to -0.6°C in September when El Niño dissipated rapidly during the spring and transitioned into La Niña during the summer. The tripole SSTA persisted from January 2010 through December 2010, and this persistence is largely attributed to the consistently negative NAO during the period from October 2009 to December 2010 (Fig. 3.3a).

The historical perspective of the 2010 SSTA is shown separately for the (a) global ocean, (b) tropical Indian Ocean, (c) tropical Pacific, (d) North Pacific, (e) tropical Atlantic, and (f) North Atlantic using OISST and ERSST in Fig. 3.4. The SSTA time series of OISST and ERSST are very similar during 1982–2010, and the similarity suggests that the SSTA signals discussed below are robust and insensitive to SST analysis techniques. The mean SSTA in the global ocean has a dominant warming trend over which are superimposed interannual variations that are largely associated with El Niño and La Niña events (Fig. 3.4a). For example, the peaks and valleys in the global ocean SSTA often correspond with those in the tropical Pacific SSTA (Fig. 3.4c). However, the correspondence is not present in 2010. The tropical Pacific SSTA cooled by 0.3°C from 2009 to 2010 under the influence of La Niña, while the global ocean SSTA remained largely the same due to a substantial warming in the tropical Atlantic (Fig. 3.4e) and a small warming in the tropical Indian Ocean (Fig. 3.4b). The tropical Indian Ocean SSTA increased by 0.17°C from 2009 to 2010, reaching a historical high in 2010, slightly higher than the value in 1998 (Fig. 3.4b). The tropical Indian Ocean SSTA is dominated by an upward trend with an increase of 0.9°C over the period 1950–2010. The interannual variations in the tropical Indian Ocean SSTA correspond well with those in the tropical Pacific SSTA due to remote influences of ENSO (Klein et al. 1999). In the tropical Atlantic, SSTA increased by 0.33°C from 2009 to 2010 and reached a historical high that is about 0.2°C higher than the previous high in 1998 (Fig. 3.4e). In contrast, there is little upward trend in the North Atlantic and North Pacific SSTA. The North Pacific SSTA trended downward from 1950 to 1987, and then rebounded from -0.5°C in 1987 to +0.31°C in 1990, and has been persistently positive since then (Fig. 3.4d). The North Atlantic SSTA has decreased from 1951 to early 1970s, and then increased and reached a historical high in 2006. It has been trending downward since 2006 (Fig. 3.4f).

There are some uncertainties in the analysis of SSTA; the 2010 SST based on OISST is about 0.4°C higher than that based on HadISST1 in the southeastern tropical Indian Ocean, Bay of Bengal, and Arabian Sea (Fig. 3.5a). The SST differences in the southeastern tropical Indian Ocean also led to uncertainties in the Indian Ocean Dipole Mode Index (DMI), defined as the SSTA differences in the western tropical Indian Ocean and southeastern tropical Indian Ocean (Saji et al. 1999). DMI was about -0.9°C during September–October in OISST but was about -0.2°C in HadISST1 (not shown). The reasons for the large SST uncertainties are suspected to be related to satellite bias adjustments, and will be investigated in the future. In addition, the OISST is generally cooler than the HadISST1 in the North Pacific and high latitude Southern Ocean (Fig. 3.5a). Differences near the western boundary currents and equatorial Pacific upwelling regions might be due to differences in resolution. The OISST and ERSST also have large differences near western boundary currents, equatorial Pacific upwelling regions, and high latitude Southern Ocean, but the two SST products agree well in the

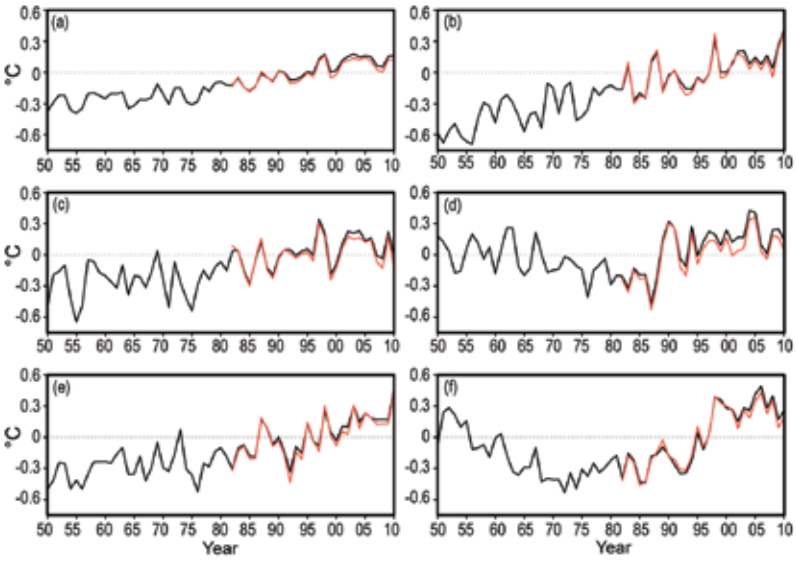

Fig. 3.4. Yearly mean SST anomalies (°C) from ERSST in 1950–2010 (black) and OISST in 1982–2010 (red) averaged in the (a) global ocean, (b) tropical Indian Ocean, (c) tropical Pacific, (d) North Pacific, (e) tropical Atlantic, (f) North Atlantic.

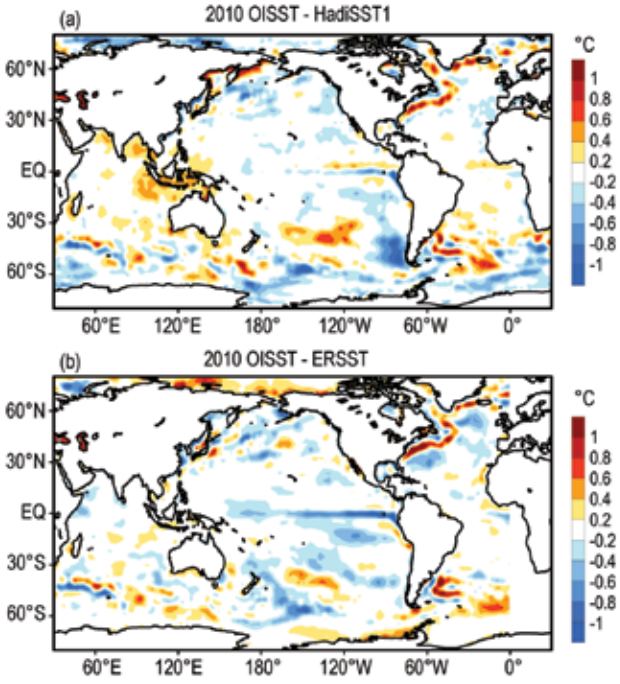

Fig. 3.5. (a) Yearly mean OISST minus HadISST1 in 2010, (b) yearly mean OISST minus ERSST in 2010.

southeastern tropical Indian Ocean and near the Maritime Continents (Fig. 3.5b).

c. Ocean heat content—G. C. Johnson, J. M. Lyman, J. K. Willis, S. Levitus, T. Boyer, J. Antonov, and S. A. Good

Storage and transport of heat in the ocean are central to aspects of climate such as El Niño (Zebiak 1989), the North Atlantic Oscillation (Curry and McCartney 2001), hurricanes (Mainelli et al. 2008), sea-level rise (Domingues et al. 2008), the global energy budget (Trenberth 2009), and constraining global warming scenarios (Knutti and Tomassini 2008).

First an estimate of upper (0 m–700 m) ocean heat content anomaly (OHCA) for the period 1 January–31 December 2010 (Fig. 3.6a) is discussed, computed from a combination of in situ ocean temperature data (Johnson et al. 2009; World Ocean Database 2009, http://www.nodc.noaa.gov/OC5/indprod.html; and Argo, Roemmich et al. 2009) and satellite altimetry data following Willis et al. (2004), but displayed relative to a 1993–2010 baseline, hereafter the combined estimate. Then changes in the combined estimate between 2010 and 2009 (Fig. 3.6b) are described, as well as maps of the linear trend of the combined estimate from 1993 to 2010 and its statistical significance (Fig. 3.7). Three different time series of global integrals of in situ-only estimates of upper OHCA are presented (Fig. 3.8). Finally, the contribution of warming deep and bottom water of Antarctic origin since the 1990s to ocean heat content is assessed. Since OHCA changes are related to depth-integrated ocean temperature changes, increases in OHCA are sometimes referred to below as warming and OHCA decreases as cooling.

In recent years, many of the globally distributed in situ subsurface ocean temperature data are from Argo. Data from Argo floats with possible uncorrected systematic pressure biases (http://www.argo.ucsd.edu/Acpres_drift_apex.html) have been removed from the combined estimate. In addition, annual estimates of expendable-bathythermograph (XBT) fall rate corrections have been applied for deep and shallow probe data using Table 2 of Wijffels et al. (2008), but with no XBT data used after 2005. Details of all the fields analyzed here may change after more Argo real-time data are subject to delayed-mode scientific quality control, as more data are reported, and as XBT corrections improve.

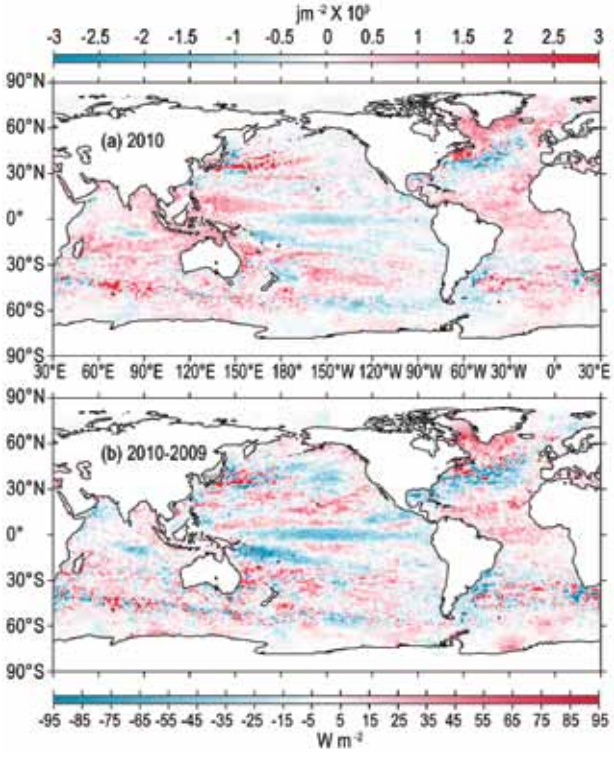

Fig. 3.6. (a) Combined satellite altimeter and in situ ocean temperature data estimate of upper (0 m–700 m) ocean heat content anomaly OHCA (10^9 J m^{-2}) for 2010 analyzed following Willis et al. (2004), but relative to a 1993–2010 baseline. (b) The difference of 2010 and 2009 combined estimates of OHCA expressed as a local surface heat flux equivalent (W m^{-2}). For panel comparisons, note that 95 W m^{-2} applied over one year results in a 3 × 10^9 J m^{-2} change of OHCA.

The combined estimate of OHCA in 2010 (Fig. 3.6a) shows eddy and meander variability down to the 100-km mapping scales, as does, to a greater extent, the difference of the 2010 and 2009 combined estimates (Fig. 3.6b). Strong small-scale spatial variability in OHCA fields is associated with the western boundary currents in every gyre, as well as the Antarctic Circumpolar Current (Fig. 3.6b). The difference in the combined estimates between 2010 and 2009 (Fig. 3.6b) illustrates the large year-to-year variability in regional ocean heat storage, with changes reaching or exceeding the equivalent of a 95 W m^{-2} magnitude surface flux applied over one year (~3×10^9 J m^{-2}). Ocean advection likely plays a dominant role in many of these changes.

Upper OHCA and salinity variability, deep OHCA and salinity variability, and mass signals all contribute to local sea level anomalies (Llovel et al. 2009). Despite these confounding factors, there are many large-scale visual similarities between the combined estimate (Fig. 3.6a) and sea level (Fig. 3.26a) fields in 2010. This similarity reflects the large contribution of upper ocean heat content variations to sea level variations.

Large-scale patterns are evident in the combined estimate of OHCA for 2010 (Fig. 3.6a) and its difference from 2009 (Fig. 3.6b). With an El Niño giving way to La Niña early in 2010, the pattern of annual mean OHCA on the Equator in the Pacific mostly reflects La Niña conditions, with a band of anomalously low values around the Equator except in the far west. In addition, a band of the lowest values in the southwest tropical Pacific since 1998 (another post-El Niño year) is found in 2010. The annual averaging period presented here is too long for detailed study of the ocean advection of heat associated with ENSO dynamics (but see Fig. 3.25 and section 4b).

The North Pacific shows a narrow band of high OHCA in the midlatitudes in 2010, perhaps associated with a Kuroshio Extension position northward of the long-term mean (see Fig. 3.21), but little else in the way of strong patterns (Fig. 3.6a). The band of high OHCA in the South Pacific that extends from the eastern Coral Sea in the west to about 50°S in the central and eastern regions (Fig. 3.6a) appears to have migrated south from tropical latitudes since 2006 (see previous *State of the Climate* reports).

Except for a small patch off Somalia and another centered near 10°S, in 2010 the Indian Ocean is mostly higher in OHCA than the baseline period (Fig. 3.6a), with that patch at 10°S and the Arabian Sea cooling between 2009 and 2010 (Fig. 3.6b). The low patch of OHCA at 10°S is associated with anomalously eastward currents to its north and anomalously westward surface currents to its south (Fig. 3.19). A zonal band of high OHCA around the Tropic of Capricorn (southern tropic) is evident in 2010. A high OHCA patch in the region west of Indonesia and extending across the Timor Sea to northern Australia also stands out in 2010.

In the subpolar North Atlantic, the Labrador and Irminger Seas are high in OHCA in 2010 (Fig. 3.6a), and have warmed quite a bit since 2009 (Fig. 3.6b). This change is consonant with strong wintertime convection in this region during early 2008 (Våge et al. 2009) being followed by warming during subsequent years with weaker winter convection. The continued high OHCA values in the eastern subpolar North Atlantic (Fig. 3.6a) suggest that subtropical influences are strong there (e.g., Johnson and Gruber 2007), consistent with anomalously salty surface conditions in that region in 2010 (Fig. 3.12a). In 2010, a band of low OHCA is evident in the region of the Gulf Stream extension, resulting from a large local cooling from 2009 to 2010. This band is consistent with a southward shift of that current (Fig. 3.19), which might be anticipated given the low North Atlantic Oscillation index in the winter of 2010 (Fig. 3.3) and pronounced local anomalies in wind stress curl (Fig. 3.27). This shift is sooner than expected given the two-year lag estimated by Taylor and Stephens (1998), but the index was quite low in winter 2009/10, and stayed low throughout 2010, which might modify the phasing. The tropical Atlantic warmed considerably from 2009 to 2010, with OHCA values higher than the mean in 2010.

A few distinct (Fig. 3.7a) and statistically significant (Fig. 3.7b) regional patterns stand out in the 1993–2010 local linear trends of OHCA. In the Indian Ocean, the warming trend is widespread, and significant. In the Atlantic Ocean, the Labrador, Irminger, and Greenland-Iceland-Norwegian Seas have all trended warmer over the interval, reflecting a robust regional warming trend over the longer time period (Fig. 3.7a) that is reinforced by the warming from 2009 to 2010 (Fig. 3.6b). These changes are probably due to an overall decrease in the North Atlantic Oscillation index from 1993 to 2010. In addition, the eastern portions of the Atlantic trend warmer across both hemispheres. As in the 2010 OHCA map, areas with warming trends appear more widespread than areas of cooling, with the latter being limited in the Atlantic to the Gulf Stream extension.

The statistically significant (Fig. 3.7b) 1993–2010

regional trends in the Pacific Ocean (Fig. 3.7a) are of warming in the western tropical Pacific and extratropical cooling in the east, consistent (via the geostrophic relation) with general strengthening of the interior subtropical-tropical circulation in the past two decades (McPhaden and Zhang 2004). The low 2010 OHCA values in the southwestern tropical Pacific (Fig. 3.6a) tend to oppose the warming trend there, but do not negate its statistical significance over the length of the record (Fig. 3.7b). The statistically significant warming in the central North Pacific and cooling south of Alaska and off the west coast of North America are also consistent with an overall downward trend in the Pacific Decadal Oscillation index from 1993 to 2010, and there is similar-looking pattern in the South Pacific.

The overall 1993–2010 trends in Southern Ocean OHCA are towards warming, consistent with previous analyses (e.g., Boning et al. 2008), but with some local cooling trends evident in the eastern Pacific and western Atlantic sectors (Fig. 3.7a).

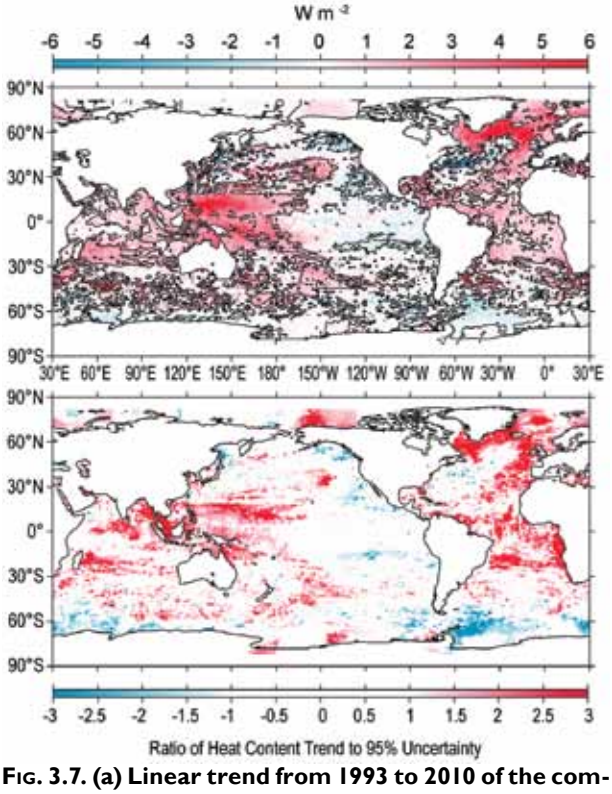

Fig. 3.7. (a) Linear trend from 1993 to 2010 of the combined satellite altimeter and in situ ocean temperature data estimate of upper (0 m–700 m) ocean heat content anomaly OHCA (W m^{-2}) analyzed following Willis et al. (2004). Areas with statistically significant trends are outlined in black. (b) Signed ratio of the linear trend to its 95% uncertainty estimate, with increasing color intensity showing regions with increasingly statistically significant trends.

Three different upper ocean estimates (0 m–700 m) of globally integrated in situ OHCA (Fig. 3.8) reveal a large increase in global integrals of that quantity since 1993. The interannual details of the time series differ for a variety of reasons including differences in climatology, treatment of the seasonal cycle, mapping methods, instrument bias corrections, quality control, and other factors (Lyman et al. 2010). Some of these factors are not taken into account in some of the displayed uncertainties, hence while the error bars shown do not always overlap among the three estimates, they are not necessarily statistically different from each other. Errors are too large to obtain reliable trends over a few years. However, the

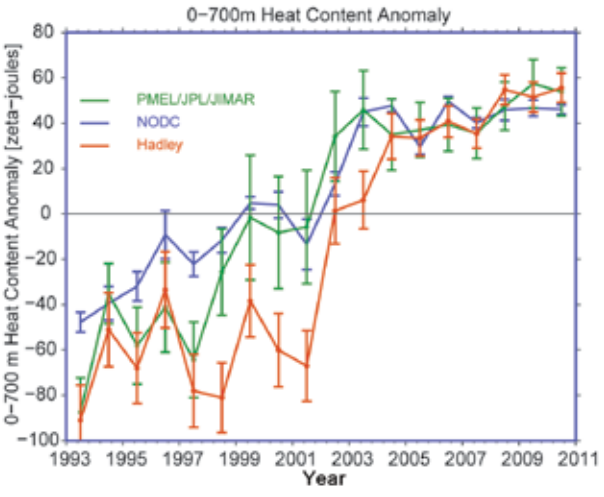

Fig. 3.8. Time series of annual average global integrals of in situ estimates of upper (0 m–700 m) OHCA (10^{21} J, or ZJ) for 1993–2010 with standard errors of the mean. The NODC estimate (http://www.nodc.noaa.gov/OC5/indprod.html) follows Levitus et al. (2009) with uncertainties derived solely from the variance of quarterly estimates of OHCA. The PMEL/JPL/JIMAR estimate is a weighted integral (Lyman and Johnson, 2008) using Argo and WOD 2009 (Johnson et al. 2009) data relative to a 2004–10 climatology with the Wijffels et al. (2008) Table 2 XBT bias adjustments applied and no XBT data after 2005 with error estimate methodology following Lyman et al. (2010). The Hadley estimate applies XBT bias adjustments from Table 1 of Wijffels et al. (2008) to the EN3 dataset (Ingleby and Huddleston 2007; http://www.metoffice.gov.uk/hadobs) also relative to a 2004–10 climatology and is computed from estimates of monthly OHCA following Palmer et al. (2007) and Palmer and Brohan (2010) with error estimate methodology similar to Rayner et al. (2006) but adding uncertainty in the XBT bias correction. For comparison, all estimates have been individually offset (vertically on the plot), first to their individual 2004–10 means (the best sampled time period), and then to their collective 1993–2010 mean (the record length).

three curves all agree on a significant decadal warming of the upper ocean since 1993, accounting for a large portion of the global energy imbalance over this time period (Trenberth 2009).

In addition to the upper (0 m–700 m) ocean warming discussed here, a number of regional studies have shown that deep and bottom waters of Antarctic origin have been warming since the early 1990s, strongest near their source, but with abyssal warming spreading north into the eastern Indian, western Atlantic, and central Pacific Oceans as summarized by Purkey and Johnson (2010). Their global synthesis of these warming changes centered on 1992–2005 estimates a trend in deep OHCA of 48 ± 32 TW (10^{12} W). The upper ocean estimates reported here have linear trends over that time period that range from 224 TW to 326 TW, therefore deep changes add a measurable fraction to the total OHCA.

d. Global ocean heat fluxes—L. Yu, X. Jin, and R. A. Weller

Latent heat (evaporation) and sensible heat fluxes (hereafter their sum is referred to as LHF+SHF) are the primary mechanism by which the oceans release much of the absorbed solar energy back to the atmosphere. These heat transfers from the ocean to the atmosphere are a cooling mechanism for the oceans but a source of heating for the atmosphere. The cooling and heating change the temperature gradients and energize the circulations in the ocean and atmosphere, which in turn affect air-sea temperature and humidity contrasts and modify the magnitudes of the ocean heat fluxes. Because of the key role air-sea heat exchange plays in the coupled atmosphere-ocean interactions and in the global energy balance, changes in global heat flux fields on short- and long-term timescales have important implications for global weather and climate patterns (e.g., Emanuel 1986; Cayan 1992).

Estimates of LHF and SHF over the global oceans are being routinely produced by the Objectively Analyzed air-sea Fluxes (OAFlux) project (http://oaflux.whoi.edu) at the Woods Hole Oceanographic Institution (Yu and Weller 2007). The computation of the OAFlux products uses the state-of-the-art bulk flux algorithm version 3.0 developed from the Coupled Ocean-Atmosphere Response Experiment (COARE; Fairall et al. 2003), with the surface meteorological variables determined from an optimal blending of satellite retrievals of surface-wind and temperatures and surface-meteorology from reanalysis/forecast models. The accuracy of the OAFlux LHF and SHF estimates was evaluated using 126 buoys available over the global oceans (Yu et al. 2008); the averaged root mean square differences between OAFlux and buoy over the buoy locations are 9.6 W m^{-2} for LHF and 2.6 W m^{-2} for SHF.

The annual-mean LHF+SHF in 2010 (Fig. 3.9a) shows that the ocean heat loss is most intense in the vicinity of the warm western boundary currents (WBCs), such as the Kuroshio off Japan, the Gulf Stream off the United States, the Agulhas Current off the African coast, the Falkland/Brazilian Current off South America, and the East Australian Current. Magnitude of the annual mean LHF+SHF in these regions exceeds 200 W m^{-2}, produced largely during the fall-to-winter seasons by strong winds and cold and dry air masses coming from the lands. Away from the WBCs, larger ocean heat loss occurs mostly over the broad subtropical oceans, with a maximum at about 20°S in the southern Indian Ocean. The air-sea heat exchange in these regions is sustained by strong trade winds in the fall/winter. The spatial

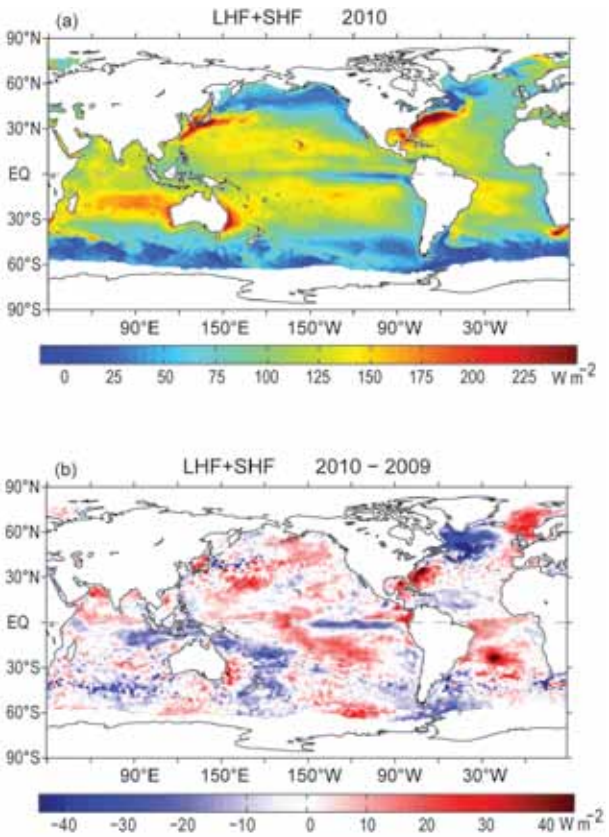

Fig. 3.9. (a) Annual mean latent plus sensible heat fluxes in 2010. The sign is defined as upward (downward) positive (negative). (b) Differences between the 2010 and 2009 annual mean latent plus sensible heat fluxes. Positive (negative) values denote an enhancement (a reduction) of ocean heat fluxes in 2010 compared to 2009.

distribution of the global LHF+SHF mean field suggests a close relationship of LHF+SHF to SST and winds (Cayan 1992).

The 2010-minus-2009 difference plot of LHF+SHF (Fig. 3.9b) shows large-scale variability over the global oceans, in which two organized patterns of change are most striking. One of such large-scale changes is the tripole structure in the North Atlantic, featuring reduced latent and sensible heat loss (negative anomalies) in the subpolar region, enhanced ocean heat loss (positive anomalies) in the middle latitudes centered off Cape Hatteras, and reduced ocean heat loss (negative anomalies) in the subtropics between the Equator and 25°N. The tripole pattern is associated with the atmospheric conditions of a persistent negative phase of NAO, which has lasted since October 2009 (Fig. 3.3a). A negative NAO state has a weak subtropical high and a weak Icelandic low. The reduced pressure gradient causes a southward displacement and weakening of the westerlies across the midlatitudes and meanwhile slackens the trade winds in the tropical oceans (Hurrell 1995; Visbeck et al. 2001). The change in wind is evident in the 2010-minus-2009 difference plot of wind speed, which is shown in Fig. 3.10 with the mean 2010 ocean-surface wind vectors at a 10 m height superimposed. Positive (negative) wind speed anomalies denote strengthening (weakening or reversing) of prevailing winds in 2010 compared with 2009. The global daily wind analysis is developed by the OAFlux project (Yu and Jin 2010) from synergizing passive radiometer wind speed retrievals and radar scatterometer vector wind retrievals. The wind analysis for the post-QuikSCAT (after November 2009) period uses satellite retrievals from the Special Sensor Microwave Imager (SSM/I), the Advanced Microwave Scanning Radiometer for EOS (AMSR-E), and the Advanced Scatterometer (ASCAT) aboard the EUMETSAT METOP satellite.

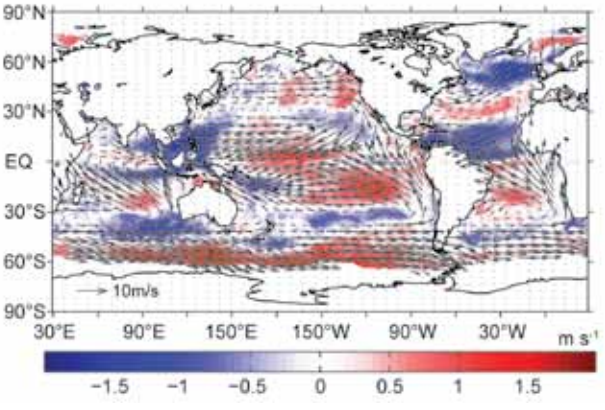

Fig. 3.10. Differences between the 2010 and 2009 wind speed at 10 m (colored background), with the 2010 mean wind vector superimposed (black arrows). Positive (negative) values denote the strengthening (weakening) of the prevailing winds compared to 2009.

The tripole pattern in the North Atlantic LHF+SHF correlates well with the NAO-induced change in the surface wind field. Positive (negative) LHF+SHF anomalies occurred in the regions of stronger (weaker) wind speeds, as wind speed facilitates the heat exchange by evaporation and conduction. Interestingly, wind direction is a more important factor. The intensified heat flux anomaly off Cape Hatteras resulted from the interaction between the warm boundary current and the cold and dry air advected by the strengthened westerlies from inland. Similarly, the large heat flux anomalies in the Norwegian Sea (north of 60°N) were due primarily to the intrusion of the cold Arctic air associated with the strengthening of the prevailing northerly winds. It is known that the basin-scale SST variability on NAO time scales is driven primarily by the atmospheric forcing via the effects of LHF+SHF, mixing, and the wind-driven Ekman currents (Cayan 1992; Deser and Blackmon 1993). It is not a surprise to see that the Atlantic sea surface had a significant warming (cooling) (Fig.3.1b) in regions of reduced (enhanced) LHF+SHF and weakened (strengthened) winds.

The other large-scale organized pattern of change in LHF+SHF is associated with the transition from El Niño to La Niña in the tropical Pacific and the coinciding development of a negative PDO in the North Pacific. Compared to 2009, the sea surface in 2010 was colder in the central and eastern equatorial basin and warmer in the western basin (Fig. 3.1b). It is interesting to observe that the correlation between SST and LHF+SHF in the tropical Pacific is not as linear as that in the North Atlantic, because LHF+SHF has reduced not only over the cooler sea surface in the east but also over the warmer sea surface in the west. That LHF+SHF decreased over the colder tongue can be explained by thermodynamic considerations. The SST in the region is controlled by ocean dynamics through wind-driven upwelling of cold water from the thermocline (Wyrtki 1981). The cold tongue became colder as the trade winds became stronger during La Niña (Fig. 3.10), which reduced the evaporation and led to a positive correlation between SST and LHF+SHF. This suggests that LHF+SHF responded to the SST anomalies in the cold tongue and acted as damping to suppress the growth of these ENSO anomalies.

On the other hand, the decrease of LHF+SHF over the warmer warm pool in the western Pacific and southeastern Indian Oceans is governed not by SST, but by atmospheric dynamics as manifested by changes in wind speed (Zhang and McPhaden 1995). Deep convection in the Indo-Pacific warm pool intensifies during La Niña (Plate 2.1g), leading to enhanced low-level convergence. By mass continuity, the center of convergence is the area of low wind speed. In 2010 both the easterlies in the central Pacific and the westerlies in the central Indian Ocean strengthened near the equatorial latitudes, while the wind speed was considerably weaker in the center of the convection over the warm pool (Fig. 3.10). It is this low wind speed that appears to have limited LHF+SHF over the warm pool. The weak LHF+SHF in turn released less heat to the atmosphere, and the weaker wind induced less mixing. Both effects caused the sea surface warming that is observed in the Indo-Pacific warm pool region (Fig.3.1b). Overall, the change in 2010 LHF+SHF in the tropical Pacific reflects more the wind speed anomalies than the SST anomalies.

The annual mean time series of the globally averaged LHF+SHF from 1958 to 2010 (Fig. 3.11) indicates that the 2010 LHF+SHF was slightly up from the 2009 mean. Nevertheless, the downward trend that started around 2000 still prevails. The 53-year time series from 1958 to 2010 displays an oscillatory nature, with a low of 99 W m^{-2} in 1977 and a high of 109 W m^{-2} in 1999. The decadal cycle is driven primarily by LHF, with minor contribution from SHF.

e. *Sea surface salinity*—G. C. Johnson and J. M. Lyman

Ocean storage and transport of freshwater are intrinsic to aspects of global climate, including the water cycle (e.g., Schanze et al. 2010), El Niño (e.g., Maes et al. 2006), and anthropogenic climate change (e.g., Held and Soden 2006). Only since 2004 has the advent of Argo allowed an annual assessment of global upper ocean salinity and its complement, freshwater. (The Argo array of profiling floats measures temperature and salinity year round in the upper 2 km of the ice-free global ocean, nominally at 10 day intervals and 3°× 3° spacing; Roemmich et al. 2009).

The near-global Argo data are used to determine an annual average sea surface salinity (SSS) anomaly for 2010 relative to a climatology and to describe how annual SSS anomalies have changed in 2010 relative to 2009, as well as to assess 2004–10 SSS trends and their statistical significance. The data, downloaded from an Argo Global Data Assembly Center in January 2011, are a mix of real-time (preliminary) and delayed mode (scientific quality controlled). The estimates of SSS presented could change after all the data have been subjected to careful scientific quality control and as other data sources are integrated into the estimates. [Remote sensing of SSS began in late 2009 with one satellite (http://www.esa.int/esaLP/LPsmos.html), with a second satellite anticipated to be launched in 2011 (http://aquarius.gsfc.nasa.gov/).]

The shallowest Argo salinity values flagged as good (excluding any with pressure > 25 dbar) are used in this analysis. They are generally at 9-dbar pressure, with some as shallow as 4 dbar. These values are subject to a statistical check to discard extreme outliers. Extreme outliers are defined as points within a 3° radius of a data point with temperature or salinity values three times the interquartile range above the third or below the first quartiles. After this check, the remaining data are cast as differences from a climatological mean surface salinity field from the World Ocean Atlas based on historical data reported through 2001 to contrast the Argo period with the earlier record (WOA 2001; Boyer et al. 2002). The resulting anomalies are objectively mapped (Bretherton et al. 1976) for each year using a covariance function combining a 6° (latitude and longitude) length-scale Gaussian with a 9° length-scale exponential and a noise-to-signal variance ratio of 2.2.

Climatological SSS patterns are correlated with surface freshwater flux: the sum of evaporation, precipitation, and river runoff (e.g., Beránger et al. 1999) where advection processes are not dominant. In each ocean basin in both the Northern and Southern Hemispheres, subtropical salinity maxima centered between

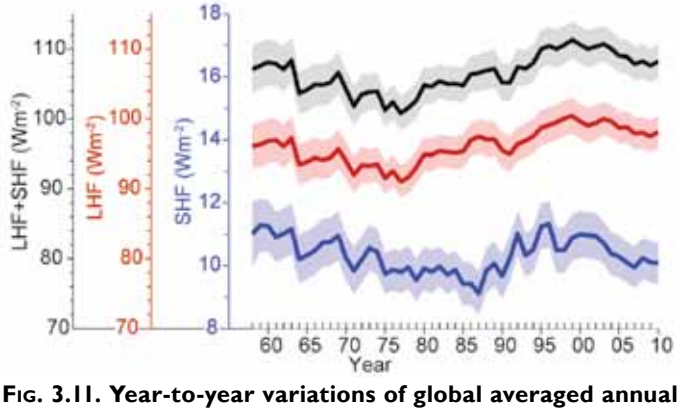

Fig. 3.11. Year-to-year variations of global averaged annual mean latent plus sensible heat flux (black curve), latent heat flux (red curve), and sensible heat flux (blue curve). The shaded areas indicate the error bars of the flux estimates at the 95% confidence level.

roughly 20° and 25° in latitude are signatures of the predominance of evaporation over precipitation. Conversely, in most regions where climatological surface salinities are relatively fresh, such as the high latitudes and the Inter Tropical Convergence Zones (ITCZs), precipitation generally dominates over evaporation.

The 2010 SSS anomalies from WOA 2001 (Fig. 3.12a) reveal some large-scale patterns that also hold in 2004 through 2009. The regions around the subtropical salinity maxima are mostly salty with respect to WOA 2001. Most of the high-latitude climatologically fresh regions appear fresher than WOA 2001, including most of the Antarctic circumpolar current near 50°S and the subpolar gyre of the North Pacific. These patterns are consistent with an increase in the hydrological cycle (that is, more evaporation in drier locations and more precipitation in rainy areas), as seen in simulations of global warming. These simulations suggest this signal might be discernible over the last two decades of the 20th century (Held and Soden 2006), consistent with the multiyear nature of these anomalies. While anomalous ocean advection could influence the SSS pattern over decadal time scales, changes observed at the local extrema are presumably relatively insensitive to such effects. The analysis presented here for SSS anomalies is supported by others: difference of maps of 2003–07 Argo data and historical 1960–89 ocean data prepared in the same fashion show a similar pattern (Hosoda et al. 2009), as do estimates of linear trends from 1950 to 2008 (Durack and Wijffels 2010; see Sidebar 3.1 for further discussion, including interior ocean trends).

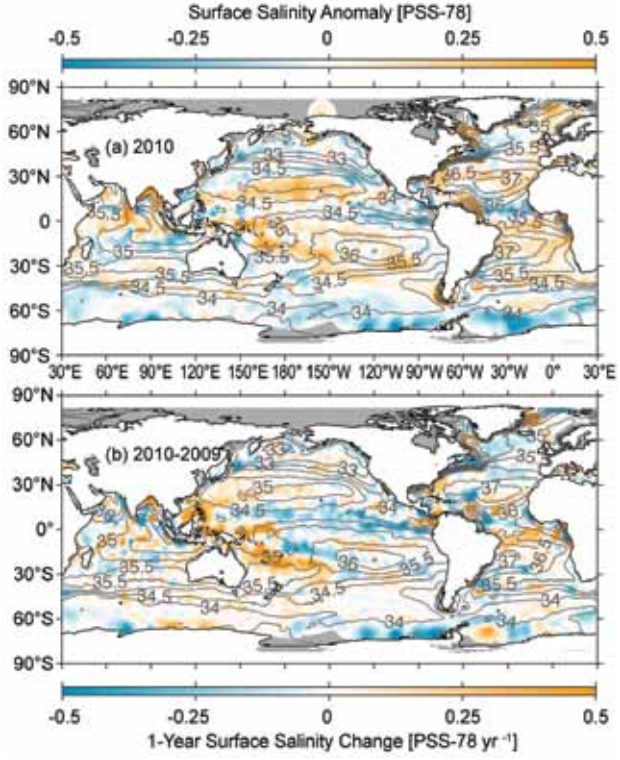

Fig. 3.12. (a) Map of the 2010 annual surface salinity anomaly estimated from Argo data [colors in 1978 Practical Salinity Scale (PSS-78)] with respect to a climatological salinity field from WOA 2001 (gray contours at 0.5 PSS-78 intervals). (b) The difference of 2010 and 2009 surface salinity maps estimated from Argo data [colors in PSS-78 yr^{-1} to allow direct comparison with (a)]. Gray areas are too data-poor to map. While salinity is often reported in practical salinity units (PSU), it is actually a dimensionless quantity reported on the PSS-78.

In contrast to the other high latitude areas, the subpolar North Atlantic and Nordic seas in 2010 are mostly anomalously salty (except east of Greenland) with respect to WOA 2001 (Fig. 3.12a), as they have been since at least 2004 (see previous *State of the Climate* reports). On the basin scale the North Atlantic loses some freshwater to the atmosphere whereas the North Pacific gains some (Schanze et al. 2010), thus the changes here may again be consistent with an increased hydrological cycle. In addition, the salty anomaly in this region is consistent with a stronger influence of subtropical gyre waters in the northeastern North Atlantic in recent years coupled with a reduced extent of the subpolar gyre (Häkkinen et al. 2011).

Sea surface salinity changes from 2009 to 2010 (Fig. 3.12b) strongly reflect 2010 anomalies in precipitation (Plate 2.1g), as well as year-to-year changes in evaporation, with the latter being closely related to latent plus sensible heat flux anomalies (Fig. 3.9b). Advection by anomalous ocean currents (Fig. 3.19) also plays a strong role in year-to-year variability of sea surface salinity. For instance, the western equatorial Pacific became considerably saltier from 2009 to 2010 while the central-eastern equatorial Pacific became fresher (Fig. 3.12b). This shift is likely partially owing to advection of salty water from the east by the anomalously westward surface currents on the Equator during that time, but an eastward shift in convection and precipitation in the equatorial Pacific during the strong El Niño in boreal winter 2009/10 also plays a large role. This pattern appears only partly compensated by the onset of La Niña later in 2010. The portion of the southwestern tropical region that became saltier in 2010 relative to 2009 may also have changed partly owing to anomalous westward surface currents. The eastern Pacific and Atlantic ITCZs also became fresher during this time period,

at least partly owing to anomalously strong precipitation in these regions during 2010. Anomalous vertical advection may also play a role in these changes, but is not analyzed here. There are strong correspondences between the surface salinity changes from 2009 to 2010 and subsurface changes over the same period (Figs. 3.14–3.16), with some of the surface changes apparently penetrating deep into the water column, suggesting influences of shifting ocean currents and fronts.

Trends from 2004 through 2010 are estimated by local linear fits to annual average SSS maps (Fig. 3.13a). The ratio of these trends to their 95% significance are also assessed (Fig. 3.13b). The starting year is 2004 because Argo coverage became near global then. The most striking trend patterns are in the Pacific. Saltier surface values in the western and central tropical Pacific extend into the eastern Pacific subtropics in both hemispheres. A strong freshening also occurs in the western subtropics of each hemisphere in the Pacific and the far western tropical Pacific, extending into the Indian Ocean northwest of Australia.

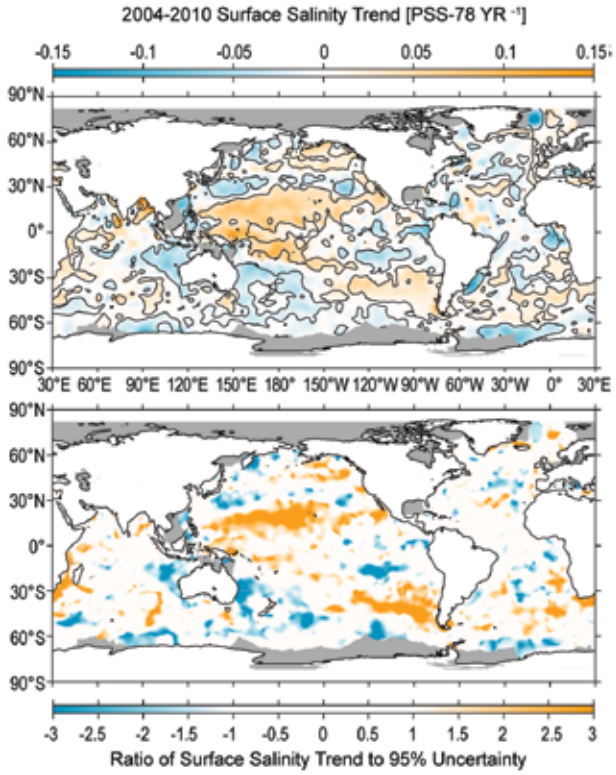

Fig. 3.13. (a) Map of local linear trends estimated from annual surface salinity anomalies for the years 2004 through 2010 estimated from Argo data (colors in PSS-78 yr^{-1}). (b) Signed ratio of the linear trend to its 95% uncertainty estimate, with increasing color intensity showing regions with increasingly statistically significant trends. Gray areas are too data-poor to map.

Large-scale freshening is also evident in the tropical Southeast Pacific. These recent trends differ from the 50-year trends discussed in the salinity sidebar of this chapter. These differences are not surprising given the very different time periods over which the trends are computed.

f. Subsurface salinity—S. Levitus, J. Antonov, T. Boyer, J. Reagan, and C. Schmid

Levitus (1989a, 1989b, 1989c), Antonov et al. (2002), Boyer et al. (2005), and Durack and Wijffels (2010) documented basin-scale changes of salinity for all or part of the world ocean on interpentadal or interdecadal time scales. Salinity changes reflect changes in the Earth's hydrological cycle and also contribute to change in sea level and ocean currents (Levitus 1990; Greatbatch et al. 1991; Sidebar 3.1).

The World Ocean Database 2009 (Boyer et al. 2009) updated through December 2010 has been used as the source of subsurface salinity data used in the analyses of 2009 and 2010 and climatological salinity conditions presented here. For 2009–10 it is primarily data from Argo profiling floats (approximately 109 000 profiles) that extend as deep as 2000 m and provide near-global coverage for the region within 60° of the Equator. Data from the TAO/TRITON, PIRATA, and RAMA arrays of tropical moored buoys provide important data in the upper 500 m of the water column. Approximately 13 000 ship-based conductivity/temperature/depth casts and 52 635 glider casts (these were highly localized in space) were also used. Final quality control has not been performed on some of the most recent observations used here, but it is not believed that additional quality control will substantially affect the results presented here. All data are available at http://www.nodc.noaa.gov.

The analysis procedure is as follows. First, monthly global analyses of salinity anomalies at standard depth levels from the sea surface to 2000 m depth are computed for years 2009 and 2010. For initial fields in the objective analyses the monthly salinity climatologies from the World Ocean Atlas 2009 (WOA09; Antonov et al. 2010) are used. Then observed data averaged on a 1° square grid at each standard depth are subtracted from the appropriate 1° climatological monthly mean. The next step is to objectively analyze (Antonov et al. 2010) these anomaly fields to generate a monthly anomaly field with an anomaly value defined at each grid point. The monthly anomaly fields are time averaged at each depth and gridpoint to define an annual mean anomaly field for each

standard depth level. This is done for 2009 and 2010.

Subsurface changes in salinity for the three major basins of the world ocean are documented in two ways. The first is to zonally average the WOA09 climatology and the 2010 annual mean field for each basin and plot these difference fields as a function of depth and latitude for the upper 1000 m of each basin as in Figs. 3.14a, 3.15a, and 3.16a. Examining these figures allows documentation of the difference in salinity conditions between 2010 and the "long-term" mean as best as can be determined with the historical data available used to construct WOA09. We only document variability in the upper 1000 m where signals are the largest and the figures can clearly document the changes that have occurred. This does not imply that changes deeper than 1000 m have not occurred, especially for the Atlantic. The second way is to document changes between these two years by zonally averaging the 2009 annual mean field by basins and plotting the 2010 minus the 2009 fields. It should be noted that it is only the advent of the Argo profiling float observing system that allows such a computation.

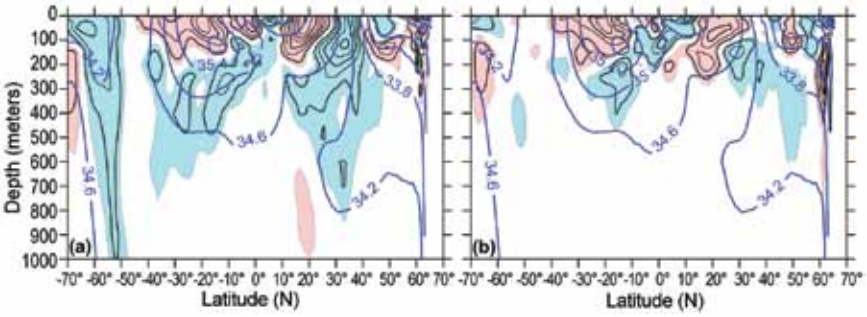

Fig 3.14. (a) Zonal mean 2010 salinity anomaly vs. latitude and depth for the Pacific Ocean. (b) Salinity anomaly 2010 minus 2009 vs. latitude and depth for the Pacific Ocean. For both plots blue shading is for areas of negative (fresh) anomaly < -0.01. Red shading is for areas of positive (salty) anomaly > 0.01. Contour interval shown for anomalies is 0.02. In the background (thick blue contours) is the zonally averaged climatological mean salinity. Contour intervals for the background are 0.4. All values are on the Practical Salinity Scale. WOA09 was used as the reference climatology for anomalies and for background means.

Figure 3.14a shows the 2010 minus climatology changes in salinity for the Pacific Ocean. There is a strong region of freshening (negative values) located in the 50°S–70°S region extending to 1000 m depth. In the 0°–45°S region there is a region of strong salinification (positive values) in the upper 200 m. This overlies a region of freshening that extends to about 700 m depth. In the 10°N–28°N region salinity has increased in the upper 125 m indicating an increase in the salinity of subtropical mode water (SMW; Yasuda and Hanawa 1997), an increase in the amount of SMW formed or both. In the 30°N–40°N region freshening occurred with the freshening extending as far south as 10°N at subsurface depths.

Figure 3.14b shows the 2010 minus 2009 changes in salinity for the Pacific Ocean. Most changes in subsurface salinity occur in the upper 400 m of this basin. At the sea surface, the 15°N–32°N region has become more saline with the positive anomaly extending south to about 10°N with increasing depth. This suggests changes in the properties of, or the amount of, SMW formed. A similar feature appears in the South Pacific centered around 20°S but with the more saline near-surface waters extending both further south and north. The subsurface high saline tongue extends northward to about 10°S. A surface freshening has occurred centered near 12°N that extends southward with increasing depth. This surface freshening may represent changes in rainfall in the Intertropical Convergence Zone (ITCZ). A relative maximum in freshening occurs centered at about 2°N at 125 m depth. This may not be directly related to changes in the ITCZ but could be linked to changes in upwelling or downwelling near the Equator which could be further linked to changes in the equatorial and tropical wind fields. Another region of subsurface freshening is centered near 12°S at 225 m depth. This might be related to changes in the tropical wind field.

Figure 3.15a shows the 2010 minus climatology changes in salinity for the Indian Ocean. Similar to the Pacific a region of freshening located in the 50°S–70°S region that extends to 1000 m depth. Immediately to the north of this feature a region (30°S–45°S) of salinification has occurred. Another region of salinification has occurred extending northward and downward from 30°S. Freshening has occurred in the 10°S–20°S region and salinification has occurred in the 10°S–12°N region.

Figure 3.15b shows the 2010 minus 2009 changes in salinity for the Indian Ocean. As in the Pacific, most changes in subsurface salinity occur in the upper 400 m of this basin. A notable exception occurs at 50°S. At 16°N and a depth of 50 m a relatively strong freshening occurred that extends to about 400 m depth. A possible explanation for this strong freshening at the

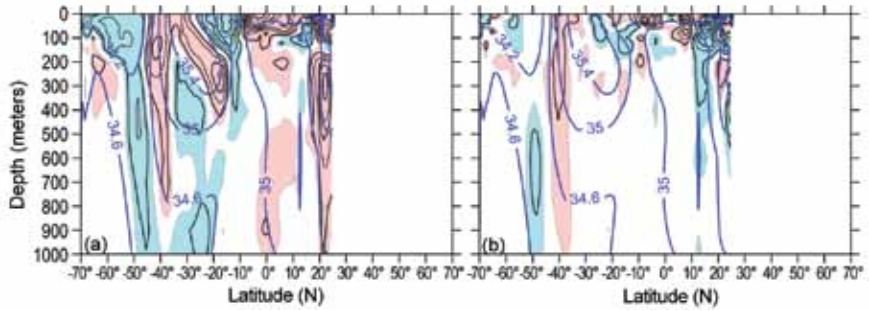

Fig 3.15. (a) Zonal mean 2010 salinity anomaly vs. latitude and depth for the Indian Ocean. (b) Salinity anomaly 2010 minus 2009 vs. latitude and depth for the Indian Ocean. For both plots blue shading is for areas of negative (fresh) anomaly < -0.01. Red shading is for areas of positive (salty) anomaly > 0.01. Contour interval shown for anomalies is 0.02. In the background (thick blue contours) is the zonally averaged climatological mean salinity. Contour intervals for the background are 0.4. All values are on the Practical Salinity Scale. WOA09 was used as the reference climatology for anomalies and for background means.

surface and deeper depths could be the ENSO impact on the Asian summer monsoon. In 2009 a strong El Niño occurred, whereas in 2010 conditions changed to a moderate-to-strong La Niña. It has been shown by Lim and Kim (2007) that during warm ENSO events (e.g., 2009), the Walker circulation in the tropical Pacific is displaced eastward resulting in higher sea level pressure in the western tropical Pacific and consequently results in subsidence over the western tropical Pacific and Indian Ocean. This pattern in turn, inhibits the ability for the monsoon to strengthen and thus less rainfall than normal falls (e.g., less freshening). Cold ENSO (e.g., 2010) events produce the reverse, with more lift in the Indian Ocean and western tropical Pacific resulting in stronger monsoons and more rainfall (e.g., more freshening). It should be noted that based on the work done by Kumar et al. (1999), this simple inverse relationship between ENSO and the Asian summer monsoon has weakened over the past two of decades. At 8°N a relatively strong increase in salinity has occurred extending to about 125 m with a similar increase in the 2°S–12°S region within the top 50 m of the water column. Another region of freshening is centered at 15°S and 100 m depth.

Figure 3.16a shows the 2010 minus climatology changes in salinity for the Atlantic Ocean. Similar to the Pacific and Indian oceans, a region of freshening occurs at high latitudes of the southern hemisphere extending to relatively deep depths (900 m). Immediately to the north is a region of salinification that is greater in magnitude than the corresponding region in the Indian Ocean. Unlike the North Pacific, the North Atlantic is characterized by an increase in salinity extending to several hundred meters depth. One exception is a very shallow region of freshening in the 0°–10°N region.

Figure 3.16b shows the 2010 minus 2009 changes in salinity for the Atlantic Ocean. Unlike the other two basins, changes in salinity have occurred to depths of 1000 m even on this one year time scale. This may be due in part to deep convection and the shifting position of large-scale fronts that have large vertical extension. Levitus (1989c) documented statistically significant large-scale changes at 1750 m depth for this basin on time scales of 20 years. Yashayaev and Loder (2009) discuss the variability of production of convectively formed Labrador Sea water. In the 60°N–70°N region, salinification has occurred that is strongest at the sea surface but extends vertically to 500 m depth. In the 50°N–60°N region, freshen-

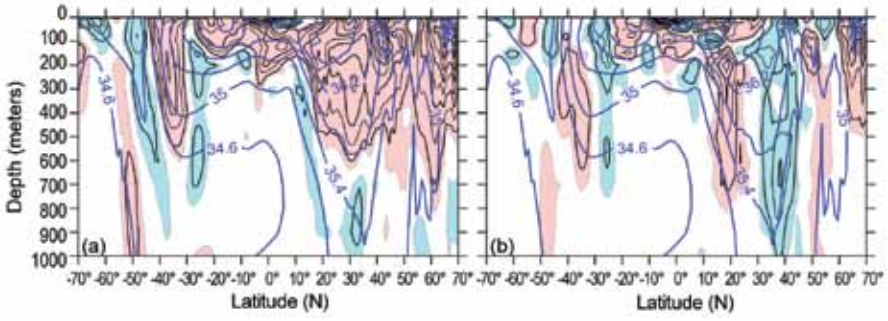

Fig 3.16. (a) Zonal mean 2010 salinity anomaly vs. latitude and depth for the Atlantic Ocean. (b) Salinity anomaly 2010 minus 2009 vs. latitude and depth for the Atlantic Ocean. For both plots blue shading is for areas of negative (fresh) anomaly < -0.01. Red shading is for areas of positive (salty) anomaly > 0.01. Contour interval shown for anomalies is 0.02. In the background (thick blue contours) is the zonally averaged climatological mean salinity. Contour intervals for the background are 0.4. All values are on the Practical Salinity Scale. WOA09 was used as the reference climatology for anomalies and for background means.

SIDEBAR 3.1: OCEAN SALINITY: A WATER CYCLE DIAGNOSTIC?—P. J. DURACK, S. E. WIJFFELS, AND N. L. BINDOFF

Present-day civilizations thrive in a wide range of temperatures at different latitudes across the Earth, but cannot cope without available freshwater. Changes to global water distribution are anticipated in the 21st century as anthropogenic climate change signatures become more apparent from natural variability of the climate system; future projections of surface moisture fluxes suggest that regions dominated by evaporation (over rainfall over the course of a year), will become drier, while regions dominated by rainfall (over evaporation) will become wetter (Allen and Ingram 2002; Held and Soden 2006; Meehl et al. 2007; Wentz et al. 2007; Seager et al. 2010). In water-stressed areas the human population and surrounding ecosystems are particularly vulnerable to decreasing or more variable rainfall due to climate change. Therefore, understanding probable future changes to the global water cycle are vital, as the projections of future climate show considerable changes to the water cycle are likely to significantly impact much of the world's population.

The global oceans cover 71% of the global surface, experience 75%–90% of global surface water fluxes, and contain 97% of the global freshwater volume (Schmitt 1995). As the ocean and land surface warms, so will the lower troposphere, and the amount of water vapor it can carry increases; this simple effect is anticipated to drive a stronger water cycle, with arid regions becoming drier and wet regions wetter (Held and Soden 2006). As the oceans are the engine room of the global water cycle, ocean salinity changes can be used to provide an estimate of broad-scale global water cycle changes and their regional patterns. Here, we review some of the major progress in understanding observed global water cycle changes in the ocean since the publication of the IPCC Fourth Assessment Report (AR4; Bindoff et al. 2007).

Global surface salinity is strongly correlated with the spatial patterns of E-P [evaporation (E) minus precipitation (P)] in the climatological mean. This relationship—where regions of low salinity correspond with regions of low (or negative) E-P and regions of high salinity with high E-P—provide some confidence in using salinity as a marker of global water cycle changes. Over long-timescales, the ocean integrates and smoothes high frequency and spatially patchy E-P fluxes at the ocean surface and provides a smoothed salinity anomaly field that facilitates detection of large-scale changes.

Patterns of long-term changes to surface salinity are now available, based on both trend fits directly to ocean data (e.g., Freeland et al. 1997; Curry et al. 2003; Boyer et al. 2005; Gordon and Giulivi 2008; Durack and Wijffels 2010) and comparisons of Argo era (2003–present) modern- to historical-ocean climatologies (e.g., Johnson and Lyman 2007; Hosoda et al. 2009; Roemmich and Gilson 2009; von Schuckmann et al. 2009; Helm et al. 2010). The patterns of multidecadal salinity change from these analyses show remarkable similarities between the mean E-P field and mean salinity field (Fig. 3.17). Rainfall-dominated regions such as the western Pacific warm pool, for example, have undergone a long-term freshening, and arid regions in the subtropical, evaporation-dominated 'desert latitudes' have generally increased in salinity (e.g., Fig. 3.17b).

Observed surface salinity changes suggest that changes in the global water cycle have occurred. The mean surface salinity climatology and the pattern of multidecadal (50-year) linear surface salinity changes (Durack and Wijffels 2010) have a spatial correlation of 0.7 (Fig. 3.18). Using this spatial relationship the amount of salinity pattern amplification can be obtained, with these data implying an amplification of the mean ocean surface salinity pattern of 8.0% has occurred between 1950 and 2000 (Fig. 3.18). In order to enhance the signal-to-noise for pattern

Continues on next page

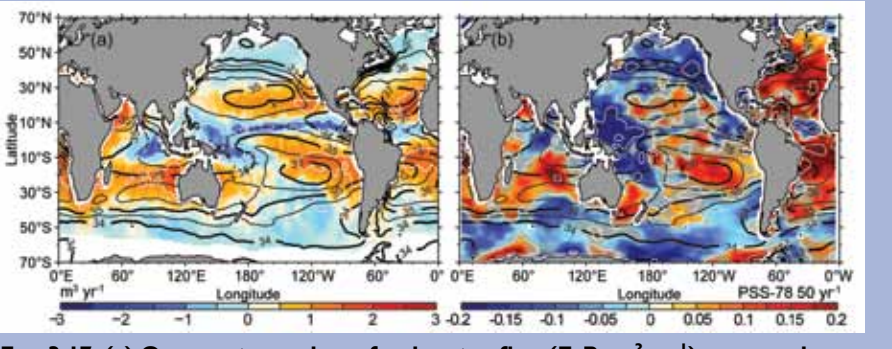

FIG. 3.17. (a) Ocean-atmosphere freshwater flux (E-P; $m^3\ yr^{-1}$) averaged over 1980–93 (Josey et al. 1998). Contours every 1 $m^3\ yr^{-1}$ in white. (b) The 50-year linear surface salinity trend (PSS-78 50 yr^{-1}). Contours every 0.25 (PSS-78) are plotted in white. On both panels, the 1975 surface mean salinity is contoured black [contour interval 0.5 (PSS-78) for thin lines, 1 for thick lines]. Due to limited observational E-P coverage a direct 1950–2000 climatology is not currently available, however the field produced by Josey et al. 1998 closely matches climatological means developed from many varied products over differing time periods (e.g. da Silva et al. 1994; Schanze et al. 2010) and provide a very similar spatial E-P pattern of correspondence with surface climatological mean salinity. Reproduced from Durack and Wijffels (2010).

amplification a spatial smoothing technique is applied to the global data; this develops basin-bound zonal means for both climatological mean salinity anomalies (compared with the global surface climatological mean salinity) and their associated 50-year salinity trends, and are termed basin-zonally-averaged means and anomalies, respectively. This robust global tendency towards an enhanced surface salinity pattern provides broad-scale agreement with the regional studies of Cravatte et al. (2009) and Curry et al. (2003), and numerous global analyses of surface salinity change (e.g., Boyer et al. 2005; Hosoda et al. 2009; Roemmich and Gilson 2009). These ocean surface salinity changes demonstrate that wet regions get fresher and dry regions saltier, following the expected response of an amplified water cycle.

Patterns of long-term subsurface salinity changes on pressure surfaces also largely follow an enhancement of the existing mean pattern. The interbasin contrast between the Atlantic (salty) and Pacific (fresh) intensifies over the observed record (e.g., Boyer et al. 2005; Johnson and Lyman 2007; Gordon and Giulivi 2008; Hosoda et al. 2009; Roemmich and Gilson 2009; von Schuckmann et al. 2009; Durack and Wijffels 2010). These deep-reaching salinity changes suggest that past water cycle changes have propagated into the ocean interior, with a clear enhancement to the high-salinity subtropical waters, and freshening of the high-latitude waters. A particularly strong and coherent freshening expressed in the Antarctic intermediate water subduction pathway centered around 50°S has also been detected (Johnson and Orsi 1997; Wong et al. 1999; Bindoff and McDougall 2000; Antonov et al. 2002; Curry et al. 2003;

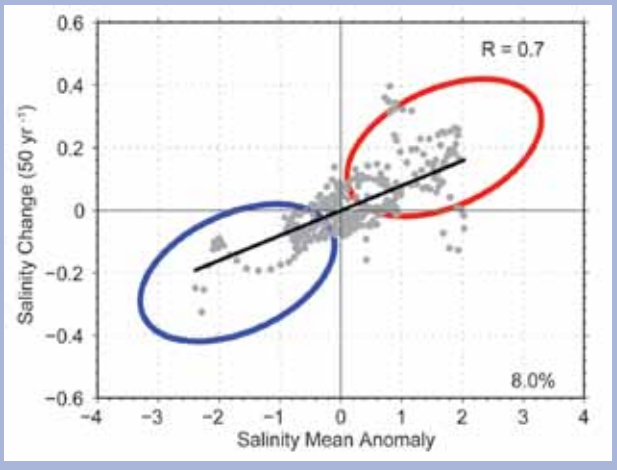

Fig. 3.18. Observed surface salinity changes versus mean salinity anomalies—fresh gets fresher and salty waters saltier. The x-axis is the basin zonally-averaged anomaly from the mean surface salinity (34.8 PSS-78), and the y-axis is the associated basin zonally-averaged multidecadal linear salinity change trend (PSS-78 50 yr^{-1}). The blue and red ellipses are representative of regions where fresh (compared to the global surface mean salinity) are getting fresher and salty getting saltier, respectively. Using the full global surface salinity analysis (Durack and Wijffels 2010), and basin-zonal mean averaging to enhance the signal-to-noise, yields a mean salinity climatology pattern amplification of 8%.

ing has occurred in the upper 100 m. A region of salinification occurs centered at 48°N. Freshening occurs in the 30°N–45°N belt extending to 1000 m depth. Salinification occurs in the upper 50 m of the 10°N–30°N belt. At 12°N, freshening occurs centered about a depth of 100 m. A belt of salinification occurs centered at 20°N between 150 m and 800 m depth. In the 0°–10°S, belt there is a region of relatively large salinification limited to approximately the upper 50 m. In the 10°S–20°S region, there is salinification suggesting an increase in SMW production or an increase in its salinity. In the region 25°S–30°S, freshening has occurred. Centered at 40°S, salinification has occurred in the 125 m–700 m layer.

g. Surface currents—R. Lumpkin, K. Dohan, and G. Goni

Near-surface currents are measured in situ by drogued satellite-tracked drifting buoys and by current meters on moored Autonomous Temperature Line Acquisition System (ATLAS) buoys.[1] During 2010, the drifter array ranged in size from a minimum of 887 drogued buoys to a maximum of 1184, with a median size of 1129 drogued buoys (undrogued drifters continue to measure SST, but are subject to significant wind slippage; Niiler et al. 1987). The moored array included 37 buoys with current meters, all between 12°S and 21°N. These tropical moorings compose the TAO/TRITON (Pacific; 16 buoys with current meters), PIRATA (Atlantic; 6 buoys) and RAMA (Indian; 15 buoys) arrays.

[1] Drifter data is distributed by NOAA/AOML at http://www.aoml.noaa.gov/phod/dac/gdp.html. Moored data is distributed by NOAA/PMEL at http://www.pmel.noaa.gov/tao. OSCAR gridded currents are available at http://www.oscar.noaa.gov/ and http://podaac.jpl.nasa.gov/. AVISO gridded altimetry is produced by SSALTO/DUACS and distributed with support from CNES, at http://www.aviso.oceanobs.com/. Analyses of altimetry-derived surface currents are available at http://www.aoml.noaa.gov/phod/altimetry/cvar.

Boyer et al. 2005; Roemmich and Gilson 2009; Hosoda et al. 2009; Durack and Wijffels 2010; Helm et al. 2010). Studies have also reported long-term and coherent salinity changes on subsurface density horizons (e.g., Wong et al. 1999; Curry et al. 2003; Helm et al. 2010). In this framework Durack and Wijffels (2010), show that many changes are dominated by subduction into the deep ocean driven by a broad-scale warming, and thus are less useful in reflecting changes in the water cycle.

In summary, several recent studies employing different analysis techniques find a clear multidecadal ocean surface salinity change. Broad-scale changes can be characterized as an amplification of the climatological salinity pattern, a tendency also found in the subsurface. The consensus view of coherent salinity change arises, even though many different analysis techniques and ocean salinity observing platforms have been used—reflecting the robustness of the signal. To first order, this suggests that broad zonal changes to E-P have changed ocean surface salinity, and changes are propagating into the subsurface ocean following the mean circulation pathways. An enhancement to mean salinity patterns and basin contrasts are the result.

How rates of salinity changes translate into rates of water cycle change remains to be determined. The ocean mixing through circulation and subduction of salinity anomalies reduces the E-P surface flux changes expressed in surface ocean salinity. Global coupled ocean-atmosphere climate models are the best tools currently available to investigate salinity and E-P change relationships, as the current observed record is too temporally and spatially sparse.

Many previous studies have used regional and global estimates of ocean salinity changes to infer water cycle changes. Hosoda et al. (2009) presented estimates of water cycle enhancement, derived from ocean salinity change trends by comparing the Argo period (2003–07) against the World Ocean Database (~1960–89). They reported an inferred global E-P enhancement of 3.7 ± 4.6% over their 30-year comparison, which considered surface salinity layer changes to 100 m depth. This enhancement is supported by the results of Trenberth et al. (2007) and Yu (2007), obtained from correlations with SST 1970–2005 (4%) and evaporation estimates 1978–2005 (~10%) respectively.

This ocean footprint of a strengthening water cycle captured in surface (and subsurface) salinity changes suggests that the remaining 29% of the global terrestrial surface has also likely experienced changes over the 1950–2000 period. Continued monitoring of future ocean property changes are necessary to effectively monitor and diagnose the effect of anthropogenic change and the rate of its evolution on our global climate system.

For homogeneous coverage and analyses such as the one presented here, ocean currents are estimated using two methodologies, both using the Archiving, Validation and Interpretation of Satellite Oceanographic data (AVISO) multimission altimeter near-real time gridded product. The first is a synthesis of AVISO with in situ drifter measurements and reanalysis winds (Niiler et al. 2003), which adjusts the altimeter-derived geostrophic velocity anomalies to match the observed in situ eddy kinetic energy. The second is the purely satellite-based OSCAR (Ocean Surface Current Analyses–Real time) product, which uses AVISO altimetry, winds, SST, and the Rio05 mean dynamic topography (Rio and Hernandez 2004) to create a 0.33°-resolution surface current maps averaged over the 0 m–30 m layer of the ocean (Bonjean and Lagerloef 2002). In both cases, anomalies are calculated with respect to the time period 1992–2007.

Global zonal current anomalies, and changes in anomalies from 2009, are shown in Figs. 3.19 and 3.20 and discussed below for individual ocean basins. In the analysis, an "eastward anomaly" is an increase in an eastward current, or a decrease in a westward current, and indicated as a positive zonal current anomaly. Similarly, negative anomalies are westward (decrease in an eastward current, or increase in a westward one).

1) Pacific Ocean

In the equatorial Pacific, 2010 began with equatorial eastward anomalies of ~50 cm s^{-1} in the center and western side of the basin, associated with the El Niño event of 2009 (Fig. 3.20). By the end of January, eastward anomalies persisted west of the dateline, but strong (30 cm s^{-1}–50 cm s^{-1}) westward anomalies had developed in the longitude band 130°W–160°W. The region of eastward anomalies propagated east across the Pacific during February through early March, while westward anomalies grew in their wake. By

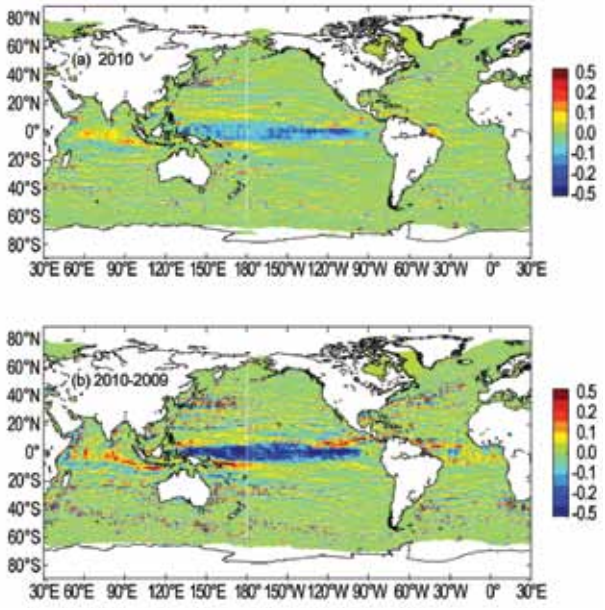

Fig. 3.19. Global zonal geostrophic anomalies for 2010 (top) and 2010 minus 2009 (bottom), cm s^{-1}, derived from a synthesis of drifters, altimetry, and winds.

April, westward anomalies were found across the entire equatorial Pacific. These anomalies reached their maximum amplitudes in mid-to-late May, with values of 60 cm s^{-1}–70 cm s^{-1} in the longitude band 110°W–140°W. This La Niña pattern persisted through boreal summer, although its amplitude diminished through this time period. The anomalous westward advection of salty water likely contributed to salty surface anomalies in the western equatorial Pacific (Fig. 3.12b). By October, the westward anomaly pattern was sufficiently weak that mesoscale patterns associated with tropical instability waves began dominating the surface current anomaly field in the region.

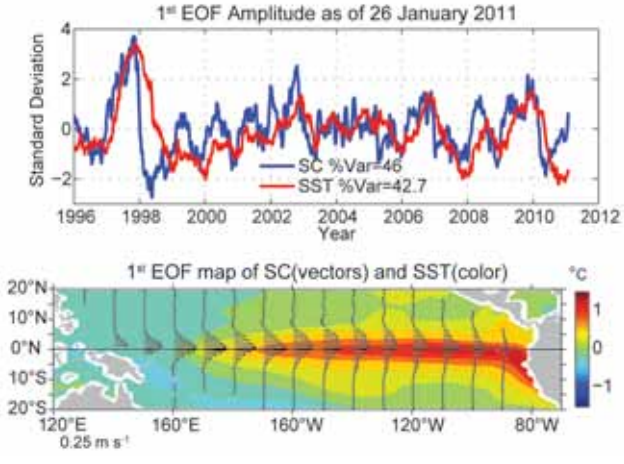

Fig. 3.20. Principal empirical orthogonal functions (EOF) of surface current (SC) and of SST anomaly variations in the tropical Pacific from the OSCAR model. Top: Amplitude time series of the EOFs normalized by their respective standard deviations. Bottom: Spatial structures of the EOFs.

Surface current anomalies in the equatorial Pacific typically lead SST anomalies by several months, with a magnitude that scales with the SST anomaly magnitude. Recovery to normal current conditions is also typically seen before SST returns to normal. Thus, current anomalies in this region are a valuable predictor of the evolution of SST anomalies and their related climate impacts. This leading nature can be seen clearly in the first principal empirical orthogonal function (EOF) of surface current anomaly and separately of SST anomaly in the tropical Pacific basin (Fig. 3.20). In mid-2010, the values of the normalized surface current and SST EOFs exceeded those of the 2000 and 2008 La Niñas, and hence by this metric, this year's La Nina was the strongest such event in the last decade.

In 2010, the Kuroshio Current exhibited a more stable path than in the last several years, with a narrower and stronger annual mean signature and a reduced area of enhanced eddy kinetic energy. Compared to 2006–09, the Kuroshio shifted approximately 1° in latitude to the north (Fig. 3.21). This shift may be related to the Kuroshio extension jet entering the strong phase of a decadal-scale fluctuation associated with the strength of the Kuroshio recirculation gyre and stability of the jet (Qiu and Chen 2005). Qiu and Chen (2005) hypothesized that this fluctuation is driven by the Pacific Decadal Oscillation (PDO), which in its negative (positive) phase generates negative (positive) sea height anomalies in the northeast Pacific which propagate to the western boundary and weaken (strengthen) the Kuroshio jet. Possibly consistent with this hypothesis, the PDO index generally dropped from 2004 to 2008 but rapidly increased through the latter part of 2009 and early 2010 (Yu and Weller 2010). However, it subsequently dropped precipitously in July 2010 (see the "Monthly Ocean Briefing" presentation by NOAA's Climate Prediction Center at http://www.cpc.ncep.noaa.gov/products/GODAS), suggesting that the northward shift may not persist through 2011.

2) Indian Ocean

Westward equatorial anomalies began developing in the western Indian Ocean in January, and by mid-February exceeded 50 cm s^{-1} at 50°E–65°E, with weaker westward anomalies from 80°E to the West African coast. This short-lived anomaly pattern was gone by the end of March. In July, weaker eastward anomalies began developing in the center and eastern side of the

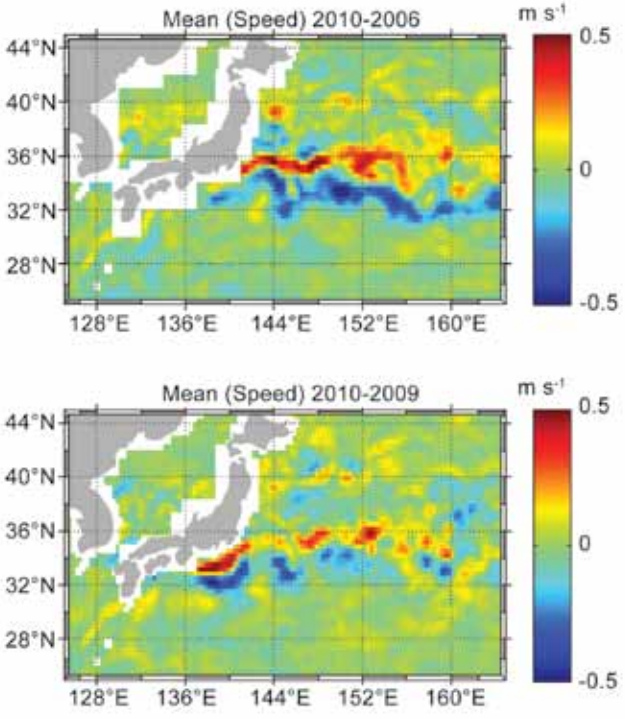

Fig. 3.21. Mean speed of the Kuroshio Current, 2010 minus 2006 (top) and 2010 minus 2009 (bottom) from OSCAR. Differences between 2010 and 2007–2008 (not shown) are similar.

basin, and were present across the basin in August–September. Eastward anomalies persisted through the remainder of the year in the center of the basin, albeit with less organization than seen in late boreal summer.

3) Atlantic Ocean

In the tropical Atlantic, near-equatorial surface currents were anomalously westward in February–April, with peak values of 20 cm s^{-1}–40 cm s^{-1} east of 30°W in mid-March, associated with anomalously cold SSTs of -0.5°C to -0.7°C at 12°W–18°W (the western half of the Atlantic cold tongue). Through boreal summer, equatorial current anomalies were less organized, although westward anomalies tended to dominate in the eastern half of the basin. In September, eastward anomalies began to develop across the basin, reaching ~25 cm s^{-1} by mid-October. These eastward anomalies persisted through November and weakened through December.

The North Brazil Current (NBC) plays an important role the Atlantic Meridional Overturning Circulation by periodically shedding rings which transfer water of Southern Hemisphere origin to the Northern Hemisphere. In 2010, the NBC demonstrated extremely anomalous conditions, with very high values of annually-averaged sea height in the ring corridor region, superimposed on the higher-frequency sea height peaks of anticyclonic rings shed from the current (Fig. 3.22). Anomalies of this magnitude have not been seen previously in the altimeter time period (1993–present).

Against the east coast of South America, the southward-flowing warm, salty Brazil Current meets the northward flowing cold, fresh Malvinas Current to create the Confluence Front. The location of this front exhibits strong fluctuations at time scales from intraseasonal and seasonal to interannual and decadal (Goni and Wainer 20001; Lumpkin and Garzoli 2010). The front shifted south approximately 1° in latitude between late 1992 and 1998, while its annual-averaged position did not change significantly from 1998 to 2009. In 2010 the annual mean location of the Confluence at the South American continental shelf break was 37.5°S, further north than has been seen since 1997. The 1992–98 trend in the Confluence location may be part of a multidecadal oscillation related to surface temperature anomalies advected from the Indian Ocean into the Atlantic via the Agulhas-Benguela pathway (Lumpkin and Garzoli 2010).

h. Meridional overturning circulation observations in the subtropical North Atlantic—M. O. Baringer, T. O. Kanzow, C. S. Meinen S. A. Cunningham, D. Rayner, W. E. Johns, H. L. Bryden, E. Faika-Williams, J. J-M. Hirschi, M. P. Chidichimo, L. M. Beal, and J. Marotzke

The meridional redistribution of mass and heat associated with the large-scale vertical circulation within an ocean basin such as the Atlantic is typically called the meridional overturning circulation (MOC).

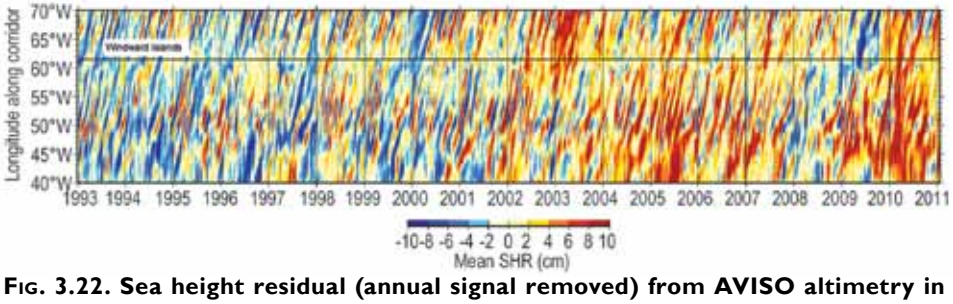

Fig. 3.22. Sea height residual (annual signal removed) from AVISO altimetry in the ring shedding corridor region of the North Brazil Current (NBC), 0°–15°N. Propagating high (red) signals indicate anticyclonic NBC rings. The longitude of the Windward Islands, which separates the Atlantic from the Caribbean, is indicated by a horizontal line.

The most common definition of the strength of the MOC is the maximum of the vertically integrated basin-wide stream function, which changes as a function of latitude and time and is influenced by many physical systems embedded within it. Substantial progress has been made on developing a coordinated observing system to begin to measure the MOC, through plans outlined at the international conference OceanObs'09 in September 2009 (e.g., Cunningham et al. 2010; Rintoul et al. 2010) and subsequent planning workshops focused on expanding existing observations to include the subpolar North and South Atlantic (e.g., Garzoli et al. 2010). A small portion of the recommended observing system has been in place since April 2004 spanning the subtropical gyre in the North Atlantic near 26.5°N. The system is composed of UK-NERC RAPID MOC moorings, US-NSF Meridional Overturning Circulation Heat-Transport Array (MOCHA), and the US-NOAA Western Boundary Time Series program (see also Chidichimo et al. 2010; Rayner et al. 2011). For the rest of the global ocean, changes in the complex, global MOC can also be inferred only from observations of individual components of the MOC (for example, a specific current or ocean layer; e.g., Dong et al. 2009), which are not discussed here.

The estimates of the MOC from the 26.5°N array include data from April 2004 to April 2009 (see also Kanzow et al. 2010). Over this time period the MOC has averaged 18.5 Sv with a high of 34.0 Sv, a low of 3.2 Sv, and a standard deviation of 4.7 Sv [using the twice daily values filtered with a 10-day cutoff as described in Cunningham et al. (2007); note Sv is a Sverdrup, equal to 10^6 m^3 s^{-1}, a unit commonly used for ocean volume transports]. These data suggest no statistically significant trend in the strength of the MOC for this extremely temporally limited dataset (-0.8 ± 1.6 Sv $decade^{-1}$, with 95% confidence limits). After five years of data, however, a clear seasonal signal is beginning to emerge (Fig. 3.23), with a low MOC in April and a high MOC in October with peak to trough range of 6.9 Sv. The MOC can be divided into three components: the northward western boundary Florida Current, the wind-driven Ekman transport, and the southward "interior" transport (upper ocean geostrophic flow between the Bahamas and Africa). The seasonal cycle of the MOC appears to be largely attributable to seasonal variability in the interior rather than Ekman or Florida Current fluctuations; Kanzow et al. (2010) show that the interior seasonal cycle is likely due to seasonal upwelling through a direct wind-driven response off Africa. Of note is that all the MOC transport values estimated from five repeated CTD (Conductivity, Temperature, Depth) sections by Bryden et al. (2005) can be found within the seasonal range of the MOC time series (values ranged from 22.9 Sv in 1957 to 14.8 Sv in 2004). In fact, Kanzow et al. (2010) demonstrated that removing the seasonal cycle estimates from Bryden et al. would effectively eliminate a statistically significant trend in the transport.

These results do not disprove the presence of a long-term trend in the strength of the MOC [e.g., Longworth et al. (2011) and Wunsch and Heimbach (2006) both found significant long-term decreases in the MOC], but they do suggest that a careful error analysis must be performed that includes the impact of the underlying higher-frequency variability of the MOC on trend estimates (see also Baehr 2010; Baehr et al. 2008; Brennan et al. 2008). Other recent studies of the MOC trend are contradictory, with some reporting a decrease in the MOC [e.g., Wunsch and Heimbach (2006), using data assimilating models; Longworth et al. (2011), using end-point hydro-

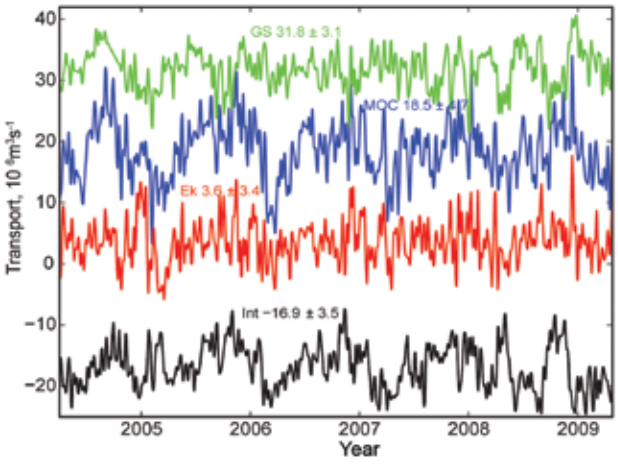

Fig. 3.23. Daily estimates of the strength of the meridional overturning circulation (MOC: blue line) and its components, the Florida Current (GS: green), wind-driven Ekman transport (Ek: red) and the geostrophic interior (Int: black), as measured by the UK National Environmental Research Council (NERC) Rapid Climate Change Program, the National Science Foundation Meridional Overturning and Heat Transport Array, and the long-term NOAA funded Western Boundary Time Series Program. The interior volume transport estimate (accurate to 1 Sv, Cunningham et al. 2007) is based on the upper ocean transport from April 2004 to April 2009 (see also Kanzow et al. 2010), with a ten-day low pass filter applied to the daily transport values. Smooth curves are the annual climatology of each component estimates from the full five years of data.

graphic observations following the 26°N mooring design principles] while others suggest no change or even an increase [e.g., Lumpkin et al. (2008), using hydrographic sections]. Some estimates showing an increase (C. Wang et al. 2010) and no trend (e.g., Schott et al. 2009) did not include basin-wide estimates of the MOC. Clearly, while disagreement remains over the details of findings from any particular observing systems (e.g., Kanzow et al. 2009), agreement exists that longer time series at multiple locations, particularly of the deep transport components, are needed (e.g., Zhang et al. 2010; Zhang 2008). New efforts are focusing on the use of state estimation models and "fingerprints" of other readily observed variables linked to changes in the MOC (e.g., Msadek et al. 2010; Lorbacher et al. 2010; Baehr 2010). Trends in the MOC can also be determined through proxies of the MOC strength, such as paleo observations (e.g., Y. Luo et al. 2010), tracers (e.g., Nelson et al. 2010; LeBel et al. 2008) and water mass characteristic (e.g. Kouketsu et al. 2009; Zhang 2008). For example, temperature and salinity observations in the Labrador Sea showed an abrupt return of deep convection between 2007 and 2008 (Våge 2009). Using water mass properties, Yashayaev and Loder (2009) showed that the enhanced deep convection in the Labrador Sea in the winter of 2008 was the deepest since 1994 and included the largest heat loss from the ocean to the atmosphere since the mid-1990s, exceeding the long term mean by 50%. Such anomalous local events may be a precursor to changes in the MOC strength (e.g., Lohmann et al. 2009).

One of the main contributions to the MOC estimate near 26.5°N is the Florida Current transport, the longest transport time series of an ocean circulation feature directly linked to the MOC. Near this latitude in the Atlantic, the bulk of the warm upper limb of the Atlantic MOC is thought to be carried to the north in the Florida Current through the Straits of Florida and the majority of the cold lower limb is believed to be carried to the south in the Deep Western Boundary Current (DWBC) just east of the Bahamas (e.g., Meinen et al. 2010; Baringer and Larsen 2001). Since 1982, Florida Current transport has been monitored using a submarine cable across the Straits of Florida in combination with regular hydrographic sections. In 2010, the mean transport through the Florida Straits continued the decrease over the past four years to 30.7 ± 1.5 Sv (95% confidence limits), lower than the 2009 31.3 ± 1.2 Sv, 2008 31.7 ± 2.2 Sv , and 2007 32.1 ± 1.0 Sv mean transports (error bars represent standard error of daily values using degrees of freedom calculated for each year, representing a typical decorrelation time scale of around 20 days). The annual mean of 2010 falls within the lowest quartile of mean annual values (32 ± 0.14 Sv). Note that while recently the annual means appear to have decreased (trend of -0.88 ± 0.85 Sv decade^{-1} from April 2004 to April 2009, 95% significance), there is only a very small significant long-term trend to the Florida Current transport (Fig 3.24; trend for full time series is -0.14 ± 0.06 Sv per decade).

The daily fluctuations of the Florida Current transport throughout the year are fairly similar to 2009 and generally fall within 90% confidence levels (Fig. 3.24). There were, however, a few unusual low transport events during the year (Fig. 3.24; the most significant or occurring over three-day or more

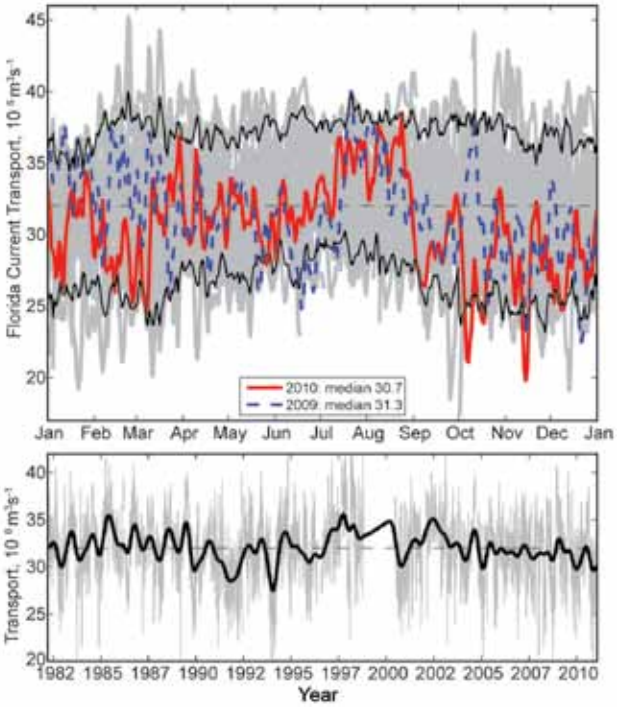

Fig. 3.24. (top) Daily estimates of the transport of the Florida Current during 2010 (red solid line) compared to 2009 (dashed blue line). The daily values of the Florida Current transport for other years since 1982 are shown in light gray and the 90% confidence interval of daily transport values computed from all years is shown in black (solid line); the long-term annual mean is dashed black. The mean transport in 2010 of 30.7 ± 1.5 Sv decreased for the fourth year in a row, below the long-term mean for the daily values of the Florida Current transport (32.2 Sv). (bottom) Daily estimates of the Florida Current transport for the full time series record (light gray), a smoothed version of transport (heavy black line; using a 30-day running mean six times) and the mean transport for the full record (dashed black).

events during 25–27 May, 5–9 October, 15–17 October, 15-17 November, and 8–10 December with values as low as 19.8 Sv). In comparison, only the transport on 24 August was higher than the 90% confidence range, with a daily average transport of 38.5 Sv. Due to the fact that these events were relatively short-lived, it is likely they are local responses to atmospheric forcing and coastally trapped wave processes and are not particularly indicative of a climatically important shift (e.g., Mooers et al. 2005). These transient fluctuations can have important environmental consequences. As examples, in the summer of 2009, the East Coast of the United States experienced a high sea-level event that was unusual due to its unexpected timing, large geographic scope, and coastal flooding that was not associated with any storms (Sweet et al. 2009). Sweet et al. (2009) showed that this anomalous event was related to the anomalously low Florida Current transport: a reduced Florida Current transport corresponds to a lower sea surface height gradient across the front and hence higher sea level onshore. In 2010, the low transport events could reasonably be inferred to have influenced sea level along the eastern U.S.; as of this report no relationship has been documented. For longer time scales, the same mechanical effect due to a reduction in ocean currents causes sea-level changes associated with geostrophy; Yin et al. (2010) showed that the dynamical response to MOC reductions associated with carbon dioxide (CO_2) emission scenarios would lead to approximately 20 cm rise in regional sea-level along the East Coast of the U.S. due to this sort of circulation change alone. Yin et al (2010) suggest that this region may be in greater jeopardy from regional effects of ocean circulation changes on top of the global mean sea-level rise predicted by climate models.

i. Sea level variations—M. Merrifield, G. Mitchum, E. Leuliette, D. Chambers, S. Nerem, P. Woodworth, S. Holgate, L. Miller, and S. Gill

Sea surface height (SSH) variations exhibited weak-to-moderate amplitudes during 2010, with the most evident patterns associated with a transition from a weak La Niña during most of 2009 to a weak El Niño (in terms of sea level) that peaked in late 2009 to early 2010 (Fig. 3.25a), returning to La Niña conditions during the remainder of 2010. In the annual mean SSH for 2010 (Fig. 3.26a), this sequence of events led to a dominant La Niña pattern in the tropical Pacific, consisting of low SSH anomalies (relative to a 1993–2010 baseline) in the central equatorial region and high SSH anomalies in the western tropical Pacific, particularly north of the Equator. SSH anomalies in other regions of the ocean that stand out in 2010 (relative to the 1993–2010 mean) include negative anomalies in the Southern Ocean to the west of South America, negative anomalies in the North Atlantic, and positive anomalies in the northwest Pacific with negative anomalies farther east (Fig. 3.26a).

The SSH tendency during 2010 is measured by the difference between the 2010 and 2009 annual means (Fig. 3.26b). The tendency in the tropical Pacific reflects the transition from El Niño to La Niña conditions, with falling SSH in the central equatorial Pacific and in the South Pacific Convergence Zone region. Other SSH tendencies of note during 2010 include negative changes in the North Pacific in the region of the Aleutian Low, with positive coastal sea level anomalies along Alaska and Canada. A similar pattern arises with falling SSH in the North Atlantic, with positive sea level anomalies along the

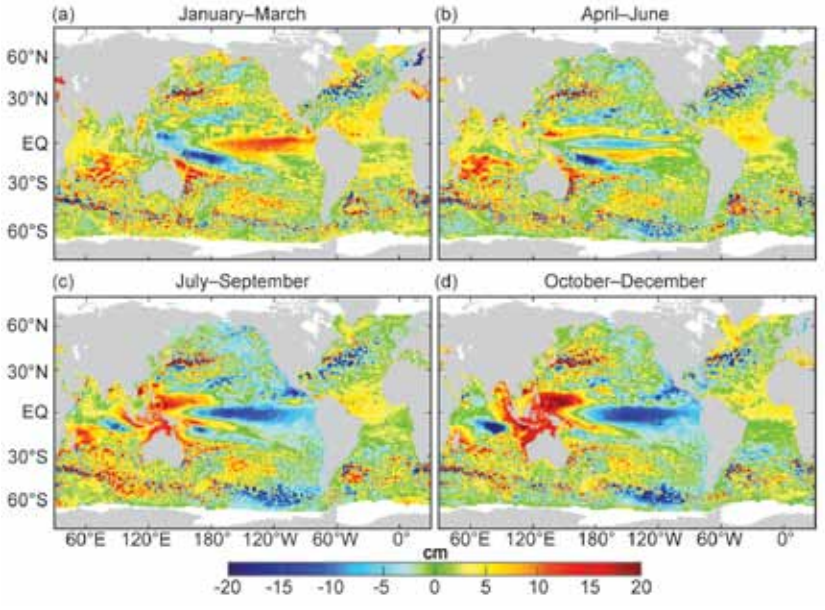

Fig. 3.25. Seasonal SSH anomalies (cm) for 2010 relative to the 1993–2010 baseline average are obtained using the multimission gridded sea surface height altimeter product produced by Ssalto/Duacs and distributed by AVISO, with support from CNES (http://www.aviso.oceanobs.com).

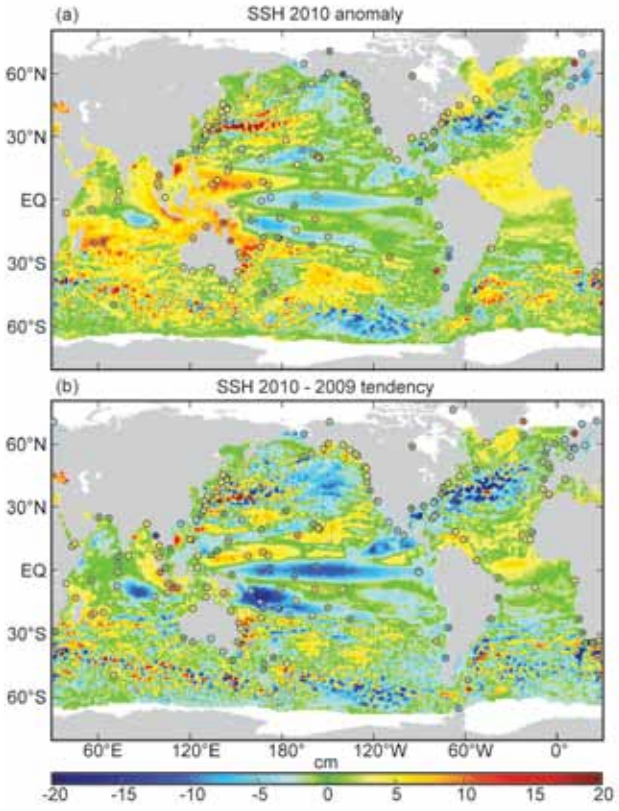

Fig. 3.26. (a) The 2010 SSH anomaly (Ssalto/Duacs product with anomaly, cm) from the 1993 to 2010 baseline is compared to the 2010 anomaly computed for tide gauge data (dots) obtained from the University of Hawaii Sea Level Center (http://uhslc.soest.hawaii.edu/). (b) The difference between 2010 and 2009 annual means (cm).

coast of the Northeast U.S. and Canada. The North Pacific pattern is associated with a deeper Aleutian Low, increasing cyclonic wind stress curl (Fig. 3.27), and lower SSH in the region of the anomalously low surface pressure. The same wind pattern accounts for greater Ekman convergence along the west coast of North America and a positive sea level tendency. These conditions are consistent with a switch toward a colder phase of the Pacific Decadal Oscillation (PDO). A similar change occurs in the North Atlantic, where the tendency from 2009 to 2010 was associated with a reduction of the midlatitude westerlies (Fig. 3.27), with an associated wind stress curl anomaly that favors lower SSH in the mid-latitude North Atlantic. The same wind change leads to Ekman convergence and higher sea levels along the east coast of North America. These conditions are consistent with a switch toward a more negative North Atlantic Oscillaion (NAO) state.

The importance of the negative PDO and NAO states during 2010 is also reflected in extreme sea level patterns. Extremes are measured here as the average of the top 2% largest daily averaged sea levels from tide gauge data. Extremes generally are larger at high latitudes (Fig. 3.28a), as is to be expected given that the extreme sea levels primarily indicate the influence of storm forcing associated with subtropical cyclones. To determine where the amplitude of extremes were below normal, normal, and above normal, we fit a generalized extreme value (GEV) distribution to the annual averages of the top 2% largest daily sea levels, using all available years at each station. The 2010 values (Fig. 3.28a) are assigned a probability based on the GEV distribution (Fig. 3.28b). The most notable region of above-average extremes (i.e., less likely occurrence and therefore low probability) is along the west coast of North America from the Aleutians all the way to San Diego (Fig. 3.28b). We attribute the above-average extremes to a combination of increased storminess during the cold PDO state, and high sea levels along the coast associated with El Niño and PDO downwelling-favorable winds. Extremes were consistently below normal in Northern Europe, which we associate with the negative NAO phase during 2010, which is characterized by a milder winter in Northern Europe.

The global rate of sea level change computed over the years 1993–2010 (Beckley et al. 2010; Leuliette and Scharroo 2010; Nerem et al. 2010) is 3.1 ± 0.4 mm yr^{-1} (one sigma). Note that the global budget of recent sea level change can be monitored by comparing total sea level measured by satellite altimeters to the sum of changes due to ocean density changes and ocean mass inputs and redistributions. For the period January 2005 to September 2010, when ocean temperature and salinity observations from the Argo float array and ocean mass variations from the Gravity Recovery

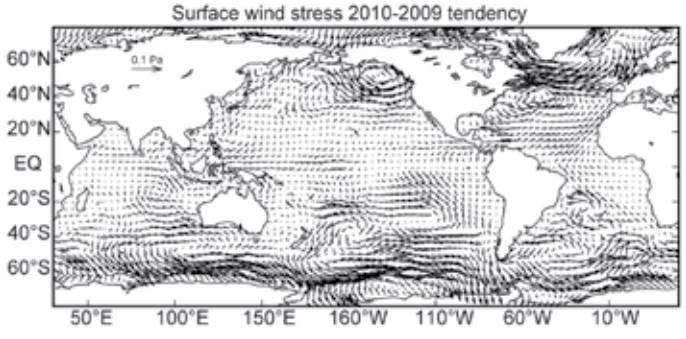

Fig. 3.27. Difference in annual mean wind stress, 2010 minus 2009. NCEP Reanalysis data provided by the NOAA/OAR/ESRL SD, http://www.esrl.noaa.gov/psd.

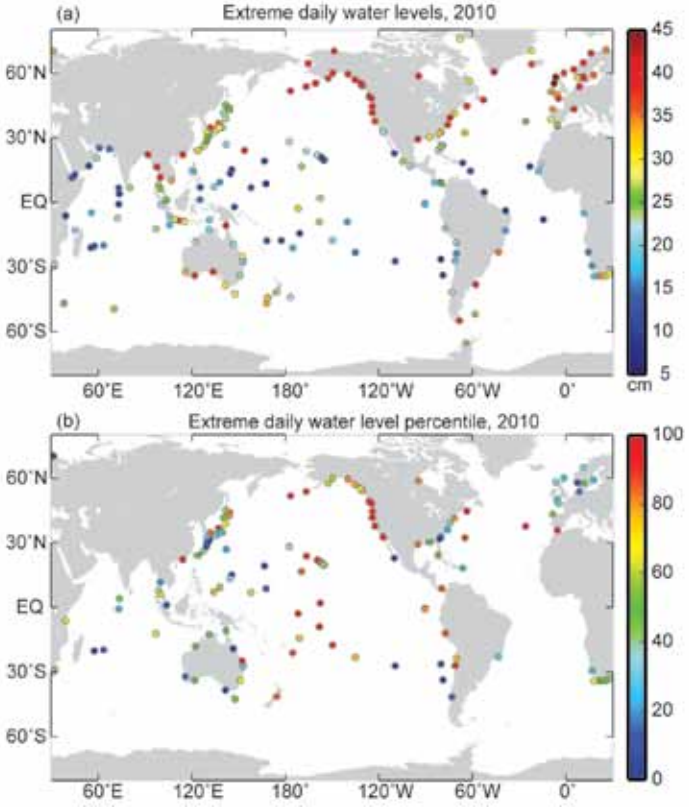

Fig. 3.28. (a) 2010 extreme sea levels measured as the average of 2% largest daily values relative the 2010 annual mean at each station. (b) Generalized extreme Value (GEV) percentiles for the 2010 extreme sea levels.

and Climate Experiment (GRACE) are available, an update to the sea level budget analyses of Leuliette and Miller (2009) and Chambers et al. (2010) shows that the recent sea level budget can be closed to within the range of uncertainties, although contribution of deep ocean heat content requires attention (see section 3c). This will be addressed in future assessments,

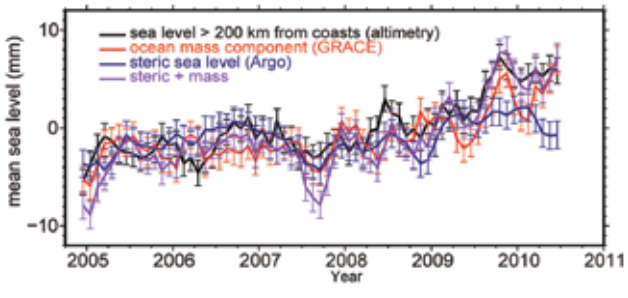

Fig. 3.29. Monthly estimates from Jason-1 and Jason-2 of global mean sea level for areas greater than 200 km from the coast (black), which are in general agreement with the sum (purple) of the ocean mass component from GRACE (red) and the steric component of the upper 700 m from Argo (blue). Seasonal signals were removed and the time series smoothed with a three-month running mean.

but for now this contribution appears to be well within the error bar. Over this brief time period and in areas more than 200 km from the nearest coast where comparisons can be made with Argo and GRACE, the mean rate of total sea level rise is 1.5 ± 0.9 mm yr^{-1} (note that the uncertainties from here to the end of this section are 95% confidence levels). This rate cannot be compared with the global average over the entire altimeter time period cited above since at least 10 years of data are required to determine a reliable rate (Nerem et al. 1999). This rate is, however, in agreement (Fig. 3.29) with the sum (1.6 ± 0.6 mm yr^{-1}) of the rates of the upper (depths < 700 m) ocean steric (0.5 ± 0.5 mm yr^{-1}) and ocean mass components (1.1 ± 0.6 mm yr^{-1}).

GRACE also allows for the monitoring of ocean mass exchange between the basins and the associated sea level change. For January 2005 to September 2010, the Indian basin shows the continued mass loss observed by Chambers and Willis (2009), equivalent to –1.3 ± 0.5 mm yr^{-1} of sea level change, while the Pacific and Atlantic have gained mass (+2.1 ± 0.5 mm yr^{-1}, +0.6 ± 0.5 mm yr^{-1}, respectively). Note that these numbers include both the mean ocean mass trend and the internal redistribution of mass. On balance, the Atlantic and Indian Oceans have been losing mass to the Pacific over this time period, but the relative contributions of fresh water inputs in each basin versus the basin-to-basin exchanges of mass are not addressed in this calculation.

In the future, total sea level changes will be understood through assessment of altimetry and tide gauges in terms of ocean density and mass changes in terms of both buoyancy and mass inputs as well as redistributions of each quantity. As of yet, the Argo and GRACE series are too short to be definitive, but in future years such analyses will be of central importance in this annual review.

j. The global ocean carbon cycle—C. L. Sabine, R. A. Feely, R. Wanninkhof, T. Takahashi, S. Khatiwala, and G.-H. Park

1. Air-sea carbon dioxide fluxes

Global surface ocean CO_2 levels are extremely variable in space and time, especially on seasonal time scales. To document the changing patterns of air-sea CO_2 exchange, an extensive observational program is required. The latest published global flux map, based on a compilation of approximately

three million measurements collected between 1970 and 2007 (hereafter referred to as LDEO), provides information on the monthly patterns of air-sea CO_2 fluxes during a "normal" non-El Niño year taken to be 2000 (Takahashi et al. 2009). The number of annual surface CO_2 observations has been growing exponentially since the 1960s such that today well over one million observations are reported to data centers each year. An update to the LDEO climatology was released in 2010 which not only includes new recent data up to 2008, but also a large number of the data from the 1957 to 1962 International Geophysical Year cruises in the Atlantic, Pacific, and Indian Oceans (Takahashi 1961; Waterman et al. 2006a, 2006b, 2006c, 2006d) thus extending the dataset by another decade (Takahashi et al. 2010).

The LDEO climatology is significant because it is directly based on in situ partial pressure of CO_2 (pCO_2) observations, but it does not provide information on how air-sea CO_2 fluxes vary from one year to the next. Annually varying global air-sea CO_2 flux estimates are based on empirical approaches relating in situ measurements with satellite observations of wind and sea surface temperature (Sabine et al. 2008, 2009, 2010). The latest empirical approach for quantifying the air-sea CO_2 exchange utilizing in situ, climatological, and satellite data from 1982 to 2007 is described in Park et al. (2010). Figure 3.30 extends these estimates through 2009. Lags in availability of quality-controlled data streams including atmospheric CO_2, satellite data, and assimilation products preclude real-time analysis such that consistent, climate-quality seasonal air-sea CO_2 flux maps are only available through 2009. The global mean air-sea CO_2 flux for the period from 1982 to 2009 using the Park et al. approach gives an average contemporary net uptake of 1.47 Pg (10^{15}g) C yr^{-1}. Following the Gruber et al. (2009) estimate that the pre-industrial steady state ocean was a source of 0.45 Pg C yr^{-1}, the estimated average net flux equates to an ocean anthropogenic CO_2 uptake of 1.92 Pg C yr^{-1}, at the lower end of the range of estimates (1.8 Pg C yr^{-1}–2.4 Pg C yr^{-1}) recently summarized by Gruber et al. (2009).

The global net CO_2 uptake flux for the 2009 transition period from La Niña to El Niño conditions (see Halpert et al. 2010) is estimated to be 1.40 Pg C yr^{-1}. During 2009, greater CO_2 uptake is found in the high northern and southern Atlantic Ocean and higher CO_2 outgassing is observed in the high northern and southern Pacific, and also the eastern Pacific Ocean compared with long-term averages (Fig. 3.31a). However, in the equatorial Pacific during the La Niña that occurred during the first half of 2009 (Fig 3.31b), the increased outgassing is offset by a decreased efflux during the El Niño that started in May–June 2009 and persisted for the remainder of the year (Fig. 3.31c). Therefore, on an annual basis, much of the equatorial Pacific shows no net anomaly (Fig. 3.30). A unique feature of the El Niño in 2009 is that the largest negative CO_2-flux anomalies occur in the central equatorial Pacific rather than in the eastern equatorial Pacific (blue colors in Fig. 3.31c). This is a direct result of greater sea surface temperature anomalies in the central equatorial Pacific than the eastern equatorial Pacific (Lee and McPhaden 2010). This change in El Niño patterns commenced in the 1990s and is referred to as El Niño Modoki. (Ashok et al. 2007).

Negative CO_2 flux anomalies found in the high-latitude Atlantic Ocean are caused primarily by increased wind speed but reinforced by SST anomalies in the region. For the high latitude Pacific Ocean, the CO_2 flux anomalies are predominantly caused by SST anomalies and partially compensated or reinforced by wind speed changes (Fig. 3.31a). Net CO_2 uptake in subtropics (42°N–42°S except the eastern equatorial Pacific) shows the second lowest value over the last 28 years (Fig. 3.30). The regional net air-sea CO_2

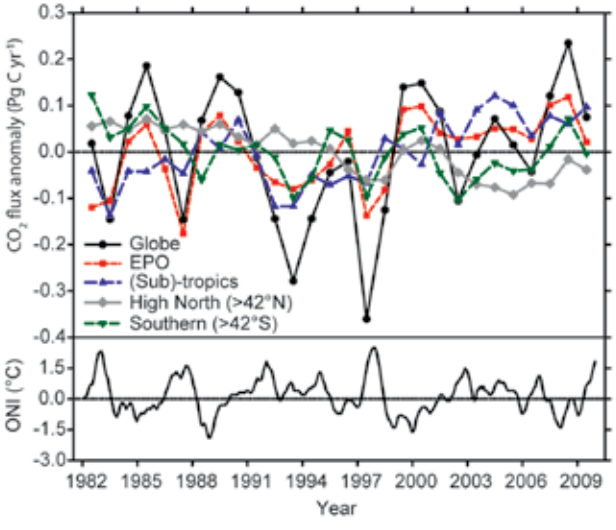

Fig. 3.30. Annual air-sea CO_2 flux anomalies 1982–2009 for the globe (black line), the equatorial Pacific Ocean (EPO; 10°N–10°S, 80°W–135°E; red dashed line), (Sub)-tropics (42°N–42°S except the EPO; blue dashed line), and high-latitude oceans (> 42°N or > 42°S; gray and green lines). The lower panel shows the Oceanic Niño Index (ONI) based on SST change in the Niño-3.4 region (Trenberth 1997). For comparison with ONI, the annual CO_2 flux anomalies are plotted in the middle of each corresponding year.

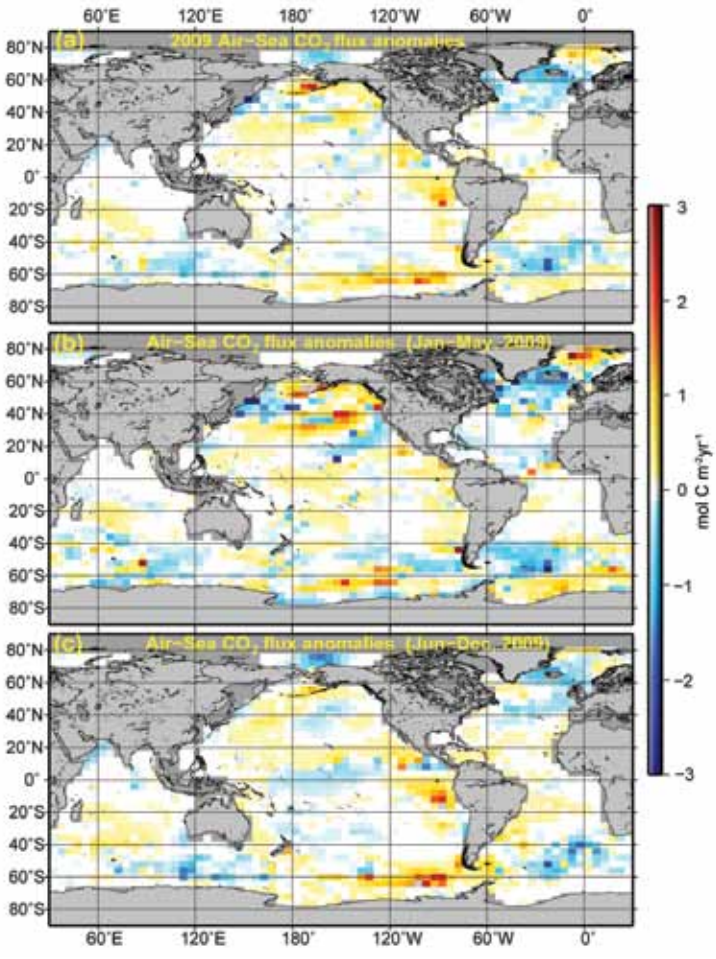

Fig. 3.31. Global distributions of air-sea CO_2 flux anomalies for the full year of 2009 (a) January to May, (b) and June to December, and (c) compared to the 28-year mean values for the corresponding months as calculated from the Park et al. (2010) approach. Positive values indicate less uptake or more release of CO_2 by the ocean[1]. The results for air-sea CO_2 flux anomalies are for the calendar year 2009 due to lags in data availability.

fluxes in 2009 in the equatorial Pacific, the Southern Ocean, and the high northern ocean are very close to 28-year mean values. The global air-sea CO_2 fluxes are closely related to the El Niño-Southern Oscillation. Higher oceanic CO_2 uptake (negative anomalies) occurs during the El Niño periods. The increase of global oceanic CO_2 uptake is not only caused by decreased CO_2 efflux in the equatorial Pacific but is also reinforced by CO_2 fluxes in the Southern Ocean and the subtropics. The monthly flux maps and anomalies from 1982 to 2009 can be created at the interactive website: http://cwcgom.aoml.noaa.gov/erddap/griddap/aomlcarbonfluxes.graph.

Implicit in the above estimates is an assumption that, at least on basin scales, the surface water pCO_2 is increasing at the same rate as the atmospheric CO_2 (i.e., ΔpCO_2 is not changing with time) and that the surface water pCO_2 is only affected by SST anomalies. The LDEO surface water pCO_2 database, with observations collected over the past three decades, reveals the mean decadal rate of increase in surface water pCO_2 in areas where sufficient number of intra- and interannual measurements are available. In Fig. 3.32, the 1981–2007 mean rates of change in sea-air pCO_2 difference (ΔpCO_2) are expressed as deviations of observed surface pCO_2 change relative to the mean rate of change in atmospheric pCO_2 of 1.68 μatm yr^{-1} (Le Quéré et al. 2010). The red circles in the North Atlantic and the red box areas in the western equatorial Pacific (Feely et al. 2006) and Southern Ocean (Takahashi et al. 2009) indicate the ocean areas where surface pCO_2 is increasing faster than the atmospheric pCO_2 and hence the ocean CO_2 sink is weakening. The blue circles indicate the ocean areas where surface pCO_2 is increasing slower than the atmospheric pCO_2 and hence the ocean CO_2 sink is intensifying. Note that the annual CO_2 flux anomalies for 2009 (from the 28-year mean; Fig. 3.31) can differ from the long-term trend of ΔpCO_2 shown in Fig. 3.32 as there is significant regional interannual variability superimposed on long-term trends. The most likely processes responsible for these observations are changes in the lateral and vertical circulation of the ocean and/or changes in marine ecosystems. Regardless of the mechanism, these data show that different ocean regions have varying responses to rising atmospheric CO_2.

2. Subsurface Carbon Inventory

In the 1990s, carbon samples were collected and analyzed from approximately 95 research cruises run as part of the international World Ocean Circulation Experiment (WOCE) and the Joint Global Ocean Flux Study (JGOFS). Based on these data, Sabine et al. (2004) estimated that the total inventory of anthropogenic CO_2 in the ocean (C_{ant}) in 1994 was 118 ± 19 Pg C, accounting for 48% of the CO_2 released from fossil fuel burning between 1800 and 1994. Since then, two approaches that heavily rely on chlorofluorocarbon data have published global inventory estimates for the reference year 1994: 94 Pg C–121 Pg C based on

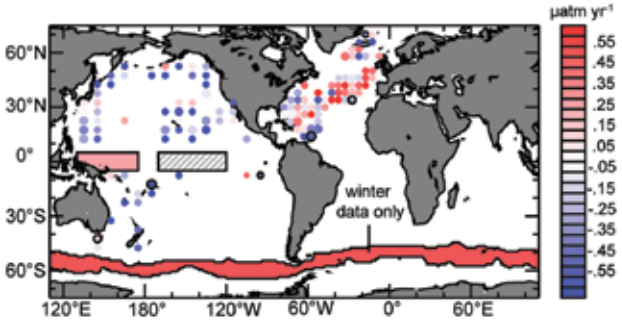

Fig. 3.32. The 1981–2007 observed rates of increase in sea-air pCO_2 difference. Red circles and areas indicate that the sea surface pCO_2 is increasing at a rate faster than the atmospheric increase rate of 1.68 µatm yr^{-1}, and hence the ocean uptake is weakening; and the blue areas show that the ocean uptake is becoming more intense. Large, medium, and small circles signify the estimated errors of < 0.25, 0.25 to 0.50, and > 0.50 µatm yr^{-1}, respectively. A single trend is shown for the Southern Ocean representing the circumpolar averaged for temperature between 0.8°C and 6.5°C using winter observations only. The gray hatched box in the central equatorial Pacific identifies the El Niño-3.4 region where observations exist but the variability is too large to clearly identify a trend (Le Quéré et al. 2010).

the TTD method (Waugh et al. 2006) and 114 ± 22 Pg C using a Green function approach (Khatiwala et al. 2009).

None of the global estimates published thus far have directly evaluated the contributions of marginal seas (defined as a semi-closed sea adjacent to a continent that is connected to the ocean), although recent work shows that several marginal seas store more C_{ant} per unit area than the global ocean and that marginal seas contribute significant C_{ant} to their adjacent major ocean basins. A key process in determining the C_{ant} uptake efficiency of these marginal seas is overturning circulation; however, the intensity of this process appears to have weakened in recent years (Lee et al. 2011). A recent synthesis of C_{ant} storage estimates for the major marginal seas suggests that as of 2008 up to 8.2 Pg C may be stored in these regions, i.e., approximately 6% of the global ocean C_{ant} storage (Lee et al. 2011). Figure 3.33 shows a compilation of these recent marginal sea estimates together with the 2008 open ocean C_{ant} distributions estimated using the approach of Khatiwala et al. (2009). This compilation gives a total ocean C_{ant} inventory estimate of 148 ± 27 Pg C for 2008. All three of the published global C_{ant} estimates assume steady state ocean circulation and use tracer information, which tends to underestimate natural variability and changes in ocean biogeochemistry. Thus, perturbations in oceanic dissolved inorganic carbon (DIC) concentrations due to anthropogenically-forced changes in large-scale circulation, ventilation, or biological activity are only partially included in these estimates.

Despite numerous technological advances over the last several decades, ship-based hydrography remains the only method for obtaining high-quality, high spatial, and vertical resolution measurements of a suite of physical, chemical, and biological parameters over the full water column. Ship-based hydrography is essential for documenting ocean changes throughout the water column, especially for the deep ocean below 2 km (52% of global ocean volume not sampled by profiling floats). Over the last decade there has been a collaborative international effort to reoccupy a subset of WOCE/JGOFS ocean survey lines to quantify changes in heat content, carbon, and anthropogenic tracers throughout the water column. A compendium of planned cruises can be found at http://www.go-ship.org/CruisePlans.html.

In late 2009 and early 2010, a zonal line (designated

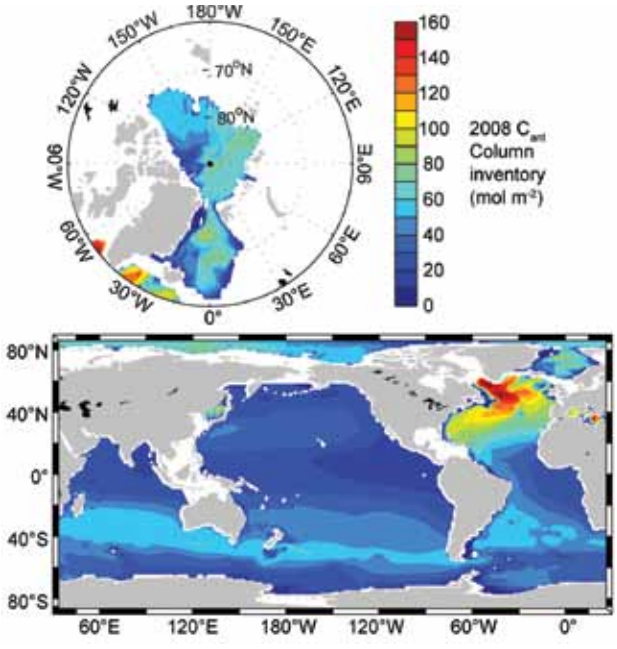

Fig. 3.33. Compilation of 2008 column inventories (mol m^{-2}) of anthropogenic CO_2 (C_{ant}): the global Ocean excluding the marginal seas (Khatiwala et al. 2009), 140 ± 25 Pg C; Arctic Ocean (Tanhua et al. 2009) 2.6 Pg C–3.4 Pg C; the Nordic seas (Olsen et al. 2010) 1.0 Pg C–1.5 Pg C; the Mediterranean Sea (Schneider et al. 2010) 1.5 Pg C–2.4 Pg C; the East Sea (Sea of Japan; Park et al. 2006) 0.40 ± 0.06 Pg C. All the marginal sea estimates were computed for 1994 and then scaled to 2008 assuming transient steady state storage of anthropogenic carbon (C_{ant}).

as P06), nominally along 32°S across the South Pacific, was completed. The top panel of Fig. 3.34 shows a section of DIC recently collected along P06. The previous occupation of that line was in 2003. The DIC from the 2003 cruise is shown in the middle panel. The bottom panel shows the difference between the two sections. To first order the DIC distributions look similar for both years, but the difference plot (Fig. 3.34, bottom) shows that DIC generally increased in the upper 500 m of the water column, presumably resulting primarily from the uptake of anthropogenic CO_2 from the atmosphere. Larger and deeper changes are observed in the eastern and western edges of the basin in association with the boundary currents in these areas. The magnitude of the changes is quite patchy with variations ranging from about -30 µmol kg^{-1} to +50 µmol kg^{-1}.

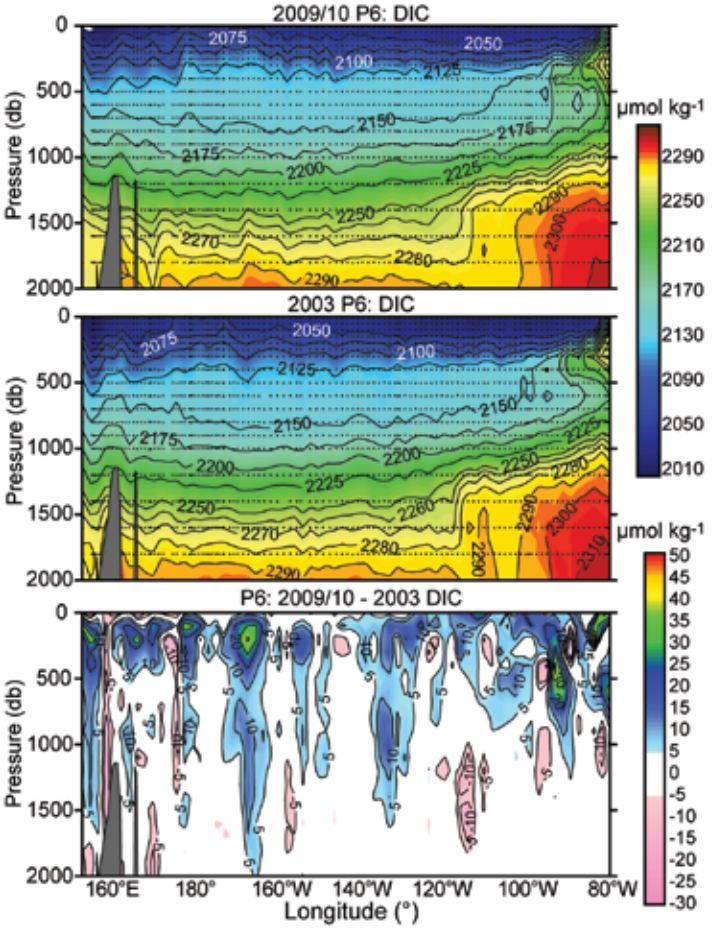

Fig. 3.34. Sections of dissolved inorganic carbon (µmol kg^{-1}) nominally along 32°S in 2009/10 conducted as part of the U.S. CLIVAR/ CO_2 Repeat Hydrography Program (top) and 2003 BEAGLE cruise conducted by the Japan Agency for Marine-Earth Science and Technology (middle). Black dots show sample locations. The bottom section shows the DIC change (µmol kg^{-1}) between the two cruises (2009/10 minus 2003).

The observed changes along P06 reflect both natural carbon variations as well as the secular anthropogenic carbon increases. Techniques are being developed to isolate the anthropogenic component of the DIC change. For example, results of a previous reoccupation of the meridional section A16, through the center of the Atlantic Ocean from Iceland to 56°S, show a clear pattern of change in CO_2 inventory between 1989 and 2005. That pattern of change, however, cannot be completely attributed to invasion of anthropogenic CO_2 (Wanninkhof et al. 2010). Concomitant large changes in dissolved oxygen suggest that processes acting on the natural carbon cycle also contribute to ΔDIC. To isolate the anthropogenic CO_2 component (ΔC_{ant}) from ΔDIC, an extended multilinear regression approach was applied along isopycnal surfaces. The change in C_{ant} inventory computed using this approach is shown in Fig. 3.35. The pattern of inventory change is qualitatively similar to the C_{ant} changes in the Atlantic since the start of the industrial era (Lee et al. 2003) with significant changes in storage in the subtropical and subpolar gyres and much smaller changes in the tropical Atlantic. An important difference between the decadal C_{ant} change compared with the total inventory, however, is that the largest accumulation of carbon over the last decade is in the South Atlantic (15°S–56°S, 0.76 mol m^{-2} yr^{-1}) as opposed to the North Atlantic (15°N–62°N, 0.57 mol m^{-2} yr^{-1}). This is opposite of the long-term trend (Fig. 3.32). This difference is attributed to reduced uptake in high northern latitudes and reduced transport of anthropogenic CO_2 northward in the Southern Hemisphere (Quay et al. 2007).

The estimated C_{ant} patterns are generally consistent with changes observed in other anthropogenic tracers (e.g., chlorofluorocarbons and pCO_2) along A16. These other tracers suggest that there is also a very small anthropogenic signal penetrating into the bottom waters (> 3500 m) from the south, but this signal seems to be too small to detect with the extended multilinear regression (eMLR) approach given the current uncertainties of the calculations. Observations and the subsequent approaches to understand the processes driving the observed changes in tracer distributions

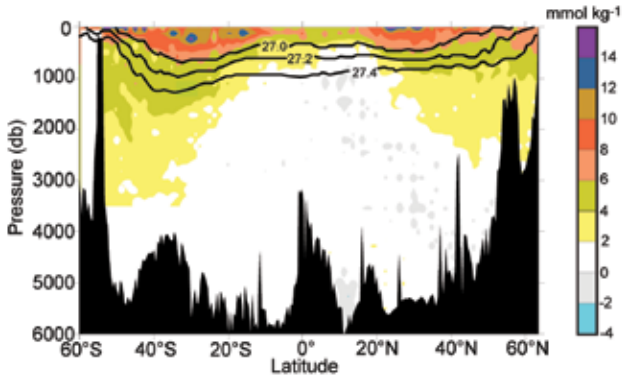

Fig. 3.35. The decadal change in anthropogenic carbon along the A16 transect. For the North Atlantic the change is between 1993 and 2003, and for the South Atlantic it is from 1989 to 2005. The estimated is based on the extended multilinear regression (eMLR) method with separate multi linear regressions (MLRs) determined for each of 23 distinct density ranges. The eMLR-based change in anthropogenic carbon is computed utilizing S, T, AOU, NO_3^-, and SiO_2 from 2003–05 as input parameters. The solid lines indicate potential density horizons, sigma-0 = 27.0, 27.2, and 27.4 kg m^{-3} (from Wanninkhof et al. 2010).

have the potential to provide a powerful constraint on the global estimates of ocean uptake and storage.

3. Global ocean phytoplankton—D. A. Siegel, M. J. Behrenfeld, S. Maritorena, R. T. O'Malley, and E. Fields

Photosynthesis by phytoplankton in the upper sunlit euphotic layer of the global ocean is the dominant source of organic matter that fuels marine ecosystems. Phytoplankton contribute roughly half of the global (land and ocean) net primary production (NPP; gross photosynthesis minus plant respiration), and phytoplankton carbon fixation is the primary conduit through which atmospheric CO_2 concentrations interact with the ocean's organic carbon pools. Phytoplankton productivity depends on the availability of sunlight, macronutrients (e.g., nitrogen and phosphorous), and micronutrients (e.g., iron), and thus is sensitive to climate-driven changes in the delivery of these resources to the euphotic zone.

Since 1997, a near-continuous record of global satellite ocean color observations has been available from the Sea viewing Wide-Field of view Sensor (SeaWiFS; McClain 2009). SeaWiFS observations have enabled investigators to address the relationships among ocean environmental conditions and phytoplankton productivity. The ecosystem property most often derived from ocean color data is surface chlorophyll concentration (Chl). Chl provides a measure of phytoplankton pigments and its variability reflects the combined influences of changes in phytoplankton biomass and its physiological responses to light and nutrient levels (e.g., Falkowski 1984; Behrenfeld et al. 2005). Figure 3.36a shows the SeaWiFS mission mean (October 1997 to November 2010) fields of Chl. Values of Chl span three orders of magnitude globally (0.03 mg m^{-3} to greater than 30 mg m^{-3}) and its spatial patterns mimic large-scale, climatological patterns in Ekman pumping and seasonal convective mixing (Sverdrup 1955; Yoder et al. 1993). Higher values of Chl are found in regions of seasonal deep mixing (e.g., North Atlantic and in the Southern Ocean) and sustained vertical upwelling (e.g., equatorial Atlantic and Pacific Oceans, off California and Peru coasts), while low values are found in the low-nutrient, permanently stratified central ocean gyres.

The SeaWiFS mission is the most consistent satellite ocean color data record ever collected (e.g., McClain 2009; NRC 2011). The entire SeaWiFS dataset has recently been reprocessed and its performance has been rigorously validated against at-sea observations (http://oceancolor.gsfc.nasa.gov/WIKI/OCReproc20100SW.html and links therein). Figure 3.36b shows the natural log (ln)-transformed Chl anomalies for the year 2010. These are calculated as the difference between monthly data for 2010 and the long-term monthly climatology and are averaged over the year 2010. Log transformations are commonly used to interpret data that vary over many orders of magnitude, and differences in ln (Chl) can be interpreted as the difference in Chl normalized by its mean value, or simply a percentage change (Campbell 1995; Boyce et al. 2010). Annual means are calculated as the composite of monthly anomalies of ln(Chl) from December 2009 through the end of November 2010 as the SeaWiFS mission ended on 14 December 2010 (http://oceancolor.gsfc.nasa.gov/forum/oceancolor/topic_show.pl?tid=3897).

Satellite chlorophyll values in 2010 show differences from the long-term mean greater than 40% in many areas (Fig. 3.36b). High Chl anomalies during 2010 occur east of Greenland, in the western equatorial Pacific, and throughout the Southern Ocean south of 55°S. Conspicuously low values of Chl during 2010 were found in the western Indian Ocean, north of Iceland, and in the eastern Atlantic off North Africa. Sea surface temperature variations for the year 2010 (Fig. 3.36c) can be characterized by: (1) a transition from El Niño to La Niña conditions during the summer 2010; (2) the development of a negative Pacific Decadal Oscillation pattern in the North Pacific during the fall/winter of 2010; and (3)

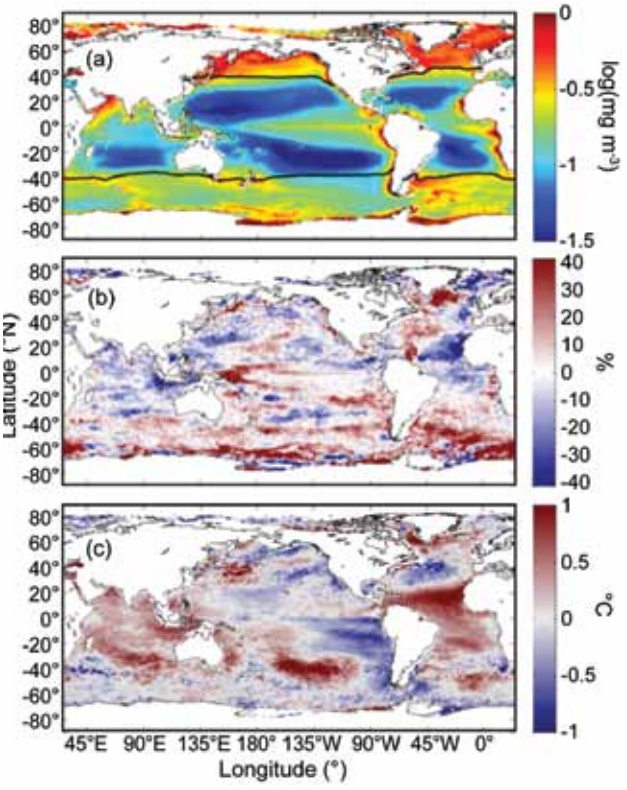

Fig. 3.36. (a) Mean Chl distribution calculated over the entire SeaWiFS record (1 November 1997 to 30 November 2010) in units of log(mg Chl m^{-3}). Also shown is the location of the mean 15°C SST isotherm (black line). Spatial distribution of anomalies for 2010 for (b) the log$_e$(Chl) (units are % difference from monthly mean) and (c) SST anomaly (units are °C). Chl anomalies are calculated using monthly OC4v6 products while SST values are from the MODIS Aqua SST4 product. Anomalies are calculated as differences in the year 2010 from monthly mean distribution for the entire SeaWiFS mission period. SST monthly means are calculated using optimally merged MODIS Aqua/Terra SST4 and AVHRR Pathfinder night-time SST products. All analyses are performed on 1° bins. The year 2010 is defined here as 1 Dec 2009 to 30 Nov 2010 as SeaWiFS ceased operating on 14 Dec 2010.

the development of a tripole SST anomaly pattern in the North Atlantic (as explained in section 3b). As seen by Behrenfeld et al. (2006), increased values of Chl generally correspond to reduced SST (and vice versa), supporting the importance of physical processes regulating global chlorophyll concentrations where changes in SST are a proxy for light, nutrient availability, and other forcing factors. In particular, a horseshoe-shaped positive Chl anomaly is observed centered on the western equatorial Pacific Ocean, indicative of an El Niño to La Niña transition (Fig. 3.36b).

The processing of SeaWiFS data makes extensive use of external standards (lunar views and intense ground efforts) to set sensor gains and offsets, and advanced algorithms to correct satellite signals for the atmospheric path radiance and establish the relationships between ocean reflectance spectra and ocean properties (McClain 2009; Ahmad et al. 2010; NRC 2011). This enables one to assess changes in Chl over its 14 years of operation. Figure 3.37 shows standardized monthly anomalies for ln(Chl) and SST aggregated over (a) the cool region of the Northern Hemisphere (NH) oceans (mean SST < 15°C), (b) the warm ocean (mean SST > 15°C), and (c) the cool region of the Southern Hemisphere (SH) oceans. (Figure 3.36a shows the location of the mean 15°C isotherm.) The sign of the SST standardized anomalies in Fig. 3.37 is flipped to accentuate the correspondence between ln(Chl) and negative SST (-SST). Broad correspondence is observed between ln(Chl) and -SST for the three regions although the only statistically significant (95% confidence interval) correlations are found for the warm ocean region where the mean SST is greater than 15°C ($R^2 = 0.19$; $p = 0.00$). An interesting feature is that the ln(Chl) and –SST anomalies appear to be coherent at low frequencies [i.e., decreases in SST correspond to increases in ln(Chl)], while on higher frequencies (many months to a few years) the cool SH region shows an inverse correlation [i.e., increases in SST correspond to increases in ln(Chl)].

A statistically significant decreasing time trend for ln(Chl) over the length of the SeaWiFS mission is found for the warm ocean region (trend = -0.19% yr^{-1}; $p = 0.01$; Fig. 3.37b), which corresponds to a significant increasing trend in SST (trend = 0.014°C yr^{-1}; $p = 0.00$). The opposing signs of these trends are consistent with ideas of a warming ocean reducing nutrient supply to the upper layers, thereby reducing phytoplankton pigment biomass (e.g., Behrenfeld et al. 2006). Significant trends are also found for the cool SH oceans (Fig. 3.37c), but are in the opposite direction compared with the warm ocean. The cool SH oceans show increasing anomalies in ln(Chl) over time (0.82% yr^{-1}; $p = 0.00$) and a cooling trend in the SST (-0.024°C yr^{-1}; $p = 0.00$). Significant time trends in ln(Chl) and SST anomalies are not found for the cool NH ocean (Fig. 3.37a).

The regional time trends presented here from the SeaWiFS mission are inconsistent with a recent analysis of centennial-scale Secchi disk and chlorophyll determinations made by Boyce et al. (2010). Boyce and his coauthors show global chlorophyll

levels decreasing over the past century at a rate nearly equal to 1% per year (as well as decreasing trends for six of eight regions in their analysis). For the warm ocean, the present trends from SeaWiFS (Fig. 3.37b) are roughly one-fifth of the centennial trends found by Boyce et al. (2010); while for the cool SH ocean, a trend of increasing chlorophyll concentrations is observed (Fig. 3.37c). Obviously, these two ocean Chl trend estimates are not evaluating the same period of time and work is needed to connect these two datasets to make a consistent long-term estimate of change in phytoplankton chlorophyll levels.

The time trends of ln(Chl) and SST are shown on local scales in Fig. 3.38. The correlation coefficient between local anomalies in ln(Chl) and SST is shown in Fig. 3.38a where significantly (95% confidence interval) positive correlations are in red and negative correlations in blue. Sites with insignificant correlation are plotted in gray. The dominant pattern here is the large degree of significant inverse correlation between local-scale ln(Chl) and SST anomalies throughout the warm ocean. Positive local-scale correlations are also found in the cool NH and SH Atlantic Ocean and for the Bering Sea.

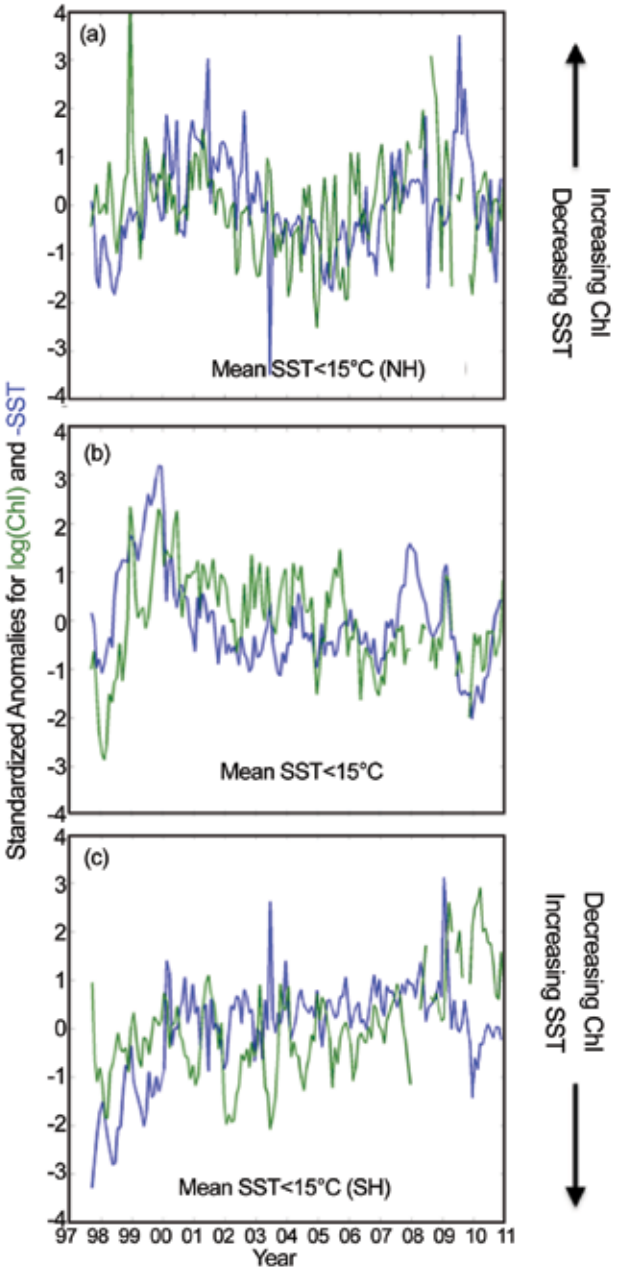

Fig. 3.37. Time series of standardized ln(Chl) (green) and negative SST (blue) monthly anomalies for (a) ocean regions of the Northern Hemisphere where the mean SST < 15°C, b) the warm ocean where mean SST values are greater than 15°C, and (c) regions of the Southern Hemisphere where the mean SST < 15°C. Anomalies are plotted in standardized form (unit variance and zero mean). SST time series are created from optimally merging MODIS Aqua/Terra SST4 and AVHRR Pathfinder products on 1° bins and monthly anomalies are summed over the three regions.

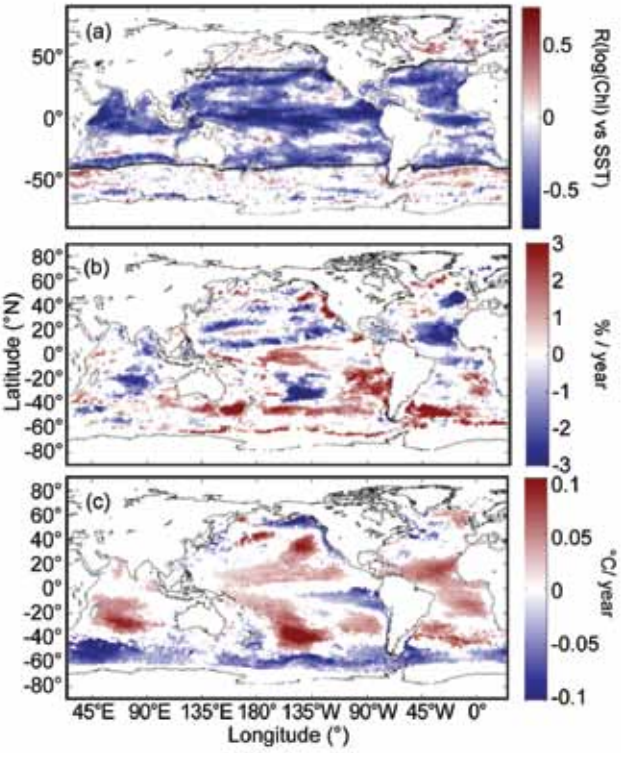

Fig. 3.38. (a) Spatial distribution of the local-scale correlation coefficient (R) between ln(Chl) and SST, (b) local-scale time trends in ln(Chl) anomalies (in % yr^{-1}), and (c) local-scale time trends in SST anomalies (in °C yr^{-1}). Only significant (95% confidence interval) correlations and trends are plotted. Calculations are made over the entire SeaWiFS record (Oct 1997–Dec 2010) and on a local-scale 1° bin in latitude and longitude. Also shown in (a) is the 15°C SST isotherm (black line).

Spatial patterns in local-scale time trends can also be examined. Local-scale trends in ln(Chl) and SST anomalies are shown in Figs. 3.38b and 3.38c, respectively. Here, regions of significantly decreasing Chl values are found throughout the warm oceans and in particular in the tropical Atlantic Ocean (Fig. 3.38b). Values of increasing Chl are found in the southern Atlantic and Pacific Oceans, the tropical Pacific, and for the eastern boundary currents of the Pacific Ocean. Local-scale SST anomaly trends show interesting patterns with significantly increasing SST within the major subtropical gyres and decreasing SST within the Southern Ocean, in the eastern Pacific, and the Gulf of Alaska (Fig. 3.38c). Clearly, the aggregated trends shown in Fig. 3.37 have many local-scale nuances and demonstrate the importance of global observations for assessing long-time changes in the oceans.

This section has focused on addressing changes seen from the SeaWiFS climate data record. The loss of this satellite, and hence the data record, creates a huge hole in observing capability and leaves open the question of how to bridge existing satellite datasets to make consistent long-term records of ocean biological properties (Siegel and Franz 2010; NRC 2011). Both NASA's MODIS Aqua and ESA's MERIS sensors are global missions and are operating well; fortunately, similar patterns in Chl are seen with MODIS Aqua observations. However SeaWiFS data were an important part of the calibrations for MODIS Aqua (see http://oceancolor.gsfc.nasa.gov/REPROCESSING/R2009/modisa_calibration) and MERIS is now being reprocessed and going through a vicarious calibration with ground data. At this point, the continuation of the climate data record initiated by SeaWiFS is not fully guaranteed as current sensors are aging and issues exist with its identified successors (e.g., NRC 2011).

Libraries: Please file with the *Bulletin of the American Meteorological Society*, Vol. 92, Issue 6